



Materials Systems Inc.

## **FLEXIBLE FABRICATION OF HIGH PERFORMANCE PIEZOELECTRIC ACTUATORS BY INJECTION MOLDING**

### **Final Report**

Contract Number: DAAH04-96-C-0089

Order Number: P-35748-EG

Report Date: 30 November 1999

Contractor:

Materials Systems Inc.  
521 Great Road  
Littleton, MA 01460

Telephone: (978) 486-0404

FAX: (978) 486-0706

E-Mail: ideas@matsysinc.com

Submitted to:

US Army Research Office  
4300 Miami Boulevard  
P.O. Box 12211  
Research Triangle Park, NC 27709-2211

Attn: Gary L. Anderson  
Ref: Contract DAAH04-96-C-0089

In fulfillment of contract requirements

**(DTC QUALITY INSPECTED 4**

20000707 075

<b>REPORT DOCUMENTATION PAGE</b>			Form Approved OMB NO. 0704-0188	
Public reporting burden for this collection of information is estimated to average 1 hour per response, including the time for reviewing instructions, searching existing data sources, gathering and maintaining the data needed, and completing and reviewing the collection of information. Send comment regarding this burden estimate or any other aspect of this collection of information, including suggestions for reducing this burden, to Washington Headquarters Services, Directorate for Information Operations and Reports, 1215 Jefferson Davis Highway, Suite 1204, Arlington, VA 22202-4302, and to the Office of Management and Budget, Paperwork Reduction Project (0704-0188), Washington, DC 20503.				
1. AGENCY USE ONLY (Leave blank)		2. REPORT DATE		3. REPORT TYPE AND DATES COVERED Final Report
4. TITLE AND SUBTITLE Flexible Fabrication of High Performance Piezoelectric Actuators by Injection Molding			5. FUNDING NUMBERS  DAAH04-96-C-0089	
6. AUTHOR(S) Craig D. Near				
7. PERFORMING ORGANIZATION NAMES(S) AND ADDRESS(ES) Materials Systems Inc. 521 Great Road Littleton, MA 01460			8. PERFORMING ORGANIZATION REPORT NUMBER	
9. SPONSORING / MONITORING AGENCY NAME(S) AND ADDRESS(ES) U.S. Army Research Office P.O. Box 12211 Research Triangle Park, NC 27709-2211			10. SPONSORING / MONITORING AGENCY REPORT NUMBER  ARO 35748.1-EG	
11. SUPPLEMENTARY NOTES The views, opinions and/or findings contained in this report are those of the author(s) and should not be construed as an official Department of the Army position, policy or decision, unless so designated by other documentation.				
12a. DISTRIBUTION / AVAILABILITY STATEMENT  Approved for public release; distribution unlimited.			12 b. DISTRIBUTION CODE	
13. ABSTRACT (Maximum 200 words)  Specific program accomplishments include: <ul style="list-style-type: none"> <li>Designed, fabricated, and tested a subscale volume actuator, offering ruggedness, high volume efficiency, and easily redirected actuation direction.</li> <li>Designed, scaled-up, fabricated, and tested over 200 unidirectional serpentine actuator elements, 25 x 25 x 1 mm in size.</li> </ul> <p style="text-align: center;">(continued on next page)</p>				
14. SUBJECT TERMS			15. NUMBER OF PAGES	
			16. PRICE CODE	
17. SECURITY CLASSIFICATION OR REPORT UNCLASSIFIED	18. SECURITY CLASSIFICATION OF THIS PAGE UNCLASSIFIED	19. SECURITY CLASSIFICATION OF ABSTRACT UNCLASSIFIED	20. LIMITATION OF ABSTRACT  UL	

REPORT DOCUMENTATION PAGE (SF298)  
(Continuation Sheet)

- Demonstrated serpentine actuator with 4 times free displacement improvement over  $d_{33}$  multilayer devices.
- Designed and evaluated an internally amplified multilayer actuator, with efficiencies as high as 24%.
- Designed, fabricated, and tested stacked co-fired multilayer actuators manufactured with MSI-53HD and PNN-1 materials.
- Developed a new high energy density actuator material, with potentially 1.7 and 2.8 times higher microstrain and energy density compared with state-of-the-art COTS piezoelectric ceramic materials.
- Showed the potential for meeting the helicopter rotorblade actuation requirements performance with the internally amplified multilayer actuator with the new high energy density material.

# INJECTION MOLDED, HIGH PERFORMANCE PIEZOELECTRIC ACTUATORS

## Contents

1.0 Executive Summary .....	1
2.0 Program Objectives .....	3
3.0 Technical Approach .....	6
4.0 Results .....	7
4.1 1-3 Piezocomposite Volume Actuator .....	7
4.2 Serpentine Element-Driven Linear Actuator.....	13
4.2.1 Serpentine Actuator Design.....	13
4.2.2 Serpentine Element .....	17
4.2.3 Serpentine Element Modeling .....	21
4.2.4 Serpentine Element Testing.....	23
4.3 Internally Amplified Multilayer Actuator.....	26
4.4 High Energy Density Actuator Materials.....	30
4.4.1 Background.....	30
4.4.2 New Material Development.....	37
4.5 Hybrid Multilayer Actuator.....	41
5.0 Conclusions.....	44
6.0 Appendices	
A. References .....	A.1
B. Presentations and Publications .....	B.1

## List of Figures

1. Boeing MD900 Explorer .....	3
2. MD900 Explorer rotorblade with integral trailing edge flap and trim tab .....	4
3. MD900 Explorer HH10 airfoil cross-section showing the forward location of the piezoelectric actuator .....	4
4. Subscale volume actuator fabricated from thirty-four 50 volume percent DOD-VI 1-3 piezocomposite elements .....	7
5. Individual 50 volume percent DOD-VI 1-3 piezocomposite elements showing silver epoxy electrodes and copper interconnect tabs .....	7
6. Thirty-four 1-3 piezocomposite elements were stacked to form the volume actuator .....	8
7. Schematic of the volume actuator located within the pressure vessel. Fill materials A, B, and C are described in Table 2 .....	8
8. Volume actuator and pressure vessel prior to assembly .....	9
9. Volume actuator sealed in pressure vessel for constrained pressure measurements at 45 Hz .....	9
10. Static volume change of unconstrained actuator .....	10
11. Output pressure from a constrained volume actuator at 45 Hz for three different fill test cases versus the predicted filler with for a 6.9 GPa bulk modulus .....	11
12. Frequency response of the nearly unconstrained case 1 volume actuator, showing an 11 kHz resonance .....	12
13. Schematic representation of serpentine PZT actuator showing typical dimensions .....	13
14. As-fired serpentine actuator fabricated by injection molding. Serpentine actuator has ~240 $\mu\text{m}$ PZT layers and ~160 $\mu\text{m}$ gaps .....	13
15. Serpentine actuator elements are stacked to form a brickwork structure to increase buckling strength. Space is left to pass the tension rod through the center of the stack .....	14

## List of Figures (cont.)

16. The linear serpentine-driven actuator was designed to use a Belleville spring to maintain a compressive preload and Kynar film and alumina plates to provide electrical insulation from the center rod and end plates .....	15
17. Amplified serpentine-driven linear actuator with 3.4:1 flextensional mechanical amplifier .....	16
18. Schematic description of the injection molding, firing, and electroding processes for serpentine element fabrication .....	17
19. Force versus displacement characteristics of medium-filled and unfilled $d_{15}$ -polarized 25 x 25 x 1 mm serpentine actuator tested at 140 V <sub>pp</sub> at 40 Hz.....	19
20. Modeling results for an unfilled $d_{33}$ -polarized serpentine element .....	21
21. MSI actuator test facility which measures voltage, current, force, displacement and their phase relationships under various static loads, mechanical impedances, temperatures, and frequencies.....	23
22. An unfilled 25 x 25 x 1 mm $d_{15}$ -polarized serpentine actuator element .....	24
23. Serpentine actuator stack consisting of three 25 x 25 x 1 mm actuator elements .....	25
24. Schematic of internally amplified multilayer actuator .....	26
25. Modeled internal flextensional amplifier designs .....	27
26. Percent change in dielectric constant and dielectric loss as a function of electric field for: DoD type I (PZT-4), DoD type II (PZT-5), and DoD type III (PZT-8) materials .....	30
27. Stress dependence of mechanical Q and Young's modulus ( $1/s_{11}^E$ ) for DoD type I (PZT-4) and DoD type II (PZT-5) materials.....	31
28. Total dissipated heat power ( $P_{DE} + P_{DM}$ ) as a function of the acoustic power ( $P_M$ ) for: DoD type I (PZT-4), DoD type II (PZT-5), and DoD type III (PZT-8) materials.....	31
29. Piezoelectric coupling factor $k_{33}$ as a function of temperature for various DoD type I materials.....	34

### **List of Figures (cont.)**

30. Microstrain capability (at 5 MV/m) as a function of temperature for various DoD type I materials .....	35
31. Blocked pressure (per unit length at 5MV/m) as a function of temperature for various DoD type I materials .....	35
32. Energy density (at 5 MV/m) as a function of temperature for various DoD type I materials .....	36
33. Dielectric constant as a function of temperature for various DoD type I and newly developed materials .....	39
34. Dielectric constant as a function of temperature for newly developed materials .....	39
35. Dielectric constant as a function of temperature for newly developed “approach 2” and PZT-4S materials, with PZT-4S Curie temperature shifted to 240°C .....	40
36. Co-fired multilayer segment fabrication process .....	42
37. A 12.7 x 12.7 x 20 mm hybrid $d_{33}$ multilayer actuator consisting of seven 25 layer co-fired segments were produced and tested A stack actuator (left) and several co-fired segments (right) are shown .....	43

## List of Tables

1. Boeing Actuation Requirements .....	5
2. Summary of Test Cases .....	10
3. Potential Improvements to Volume Actuator .....	11
4. Actuation Displacement Performance Comparison between Standard $d_{31}$ Plate, Standard $d_{33}$ Multilayer, and Two Serpentine Actuator Configurations.....	18
5. Average Tensile Properties of Candidate Fill and Encapsulant Materials .....	18
6. Actuator Limits and Compressional Operating Conditions for 12.5 x 12.5 x 1.0 mm $d_{33}$ -Polarized Serpentine Element at 140 V <sub>pp</sub> .....	19
7. Actuation Performance Comparison between Standard $d_{31}$ Plates, Standard $d_{33}$ Multilayer, and Two Serpentine Actuator Configurations.....	20
8. Summary of Measured and Modeled Longitudinal Displacements.....	21
9. Comparison between Actual and Modeled 25 x 25 x 1 mm $d_{15}$ -Polarized Serpentine Actuator Performance for Various Gap Overlaps at 140 V <sub>pp</sub> .....	22
10. Performance of Candidate Internally Amplified Actuators.....	28
11. PZT Isovalent Additions.....	32
12. Perovskite Crystal Parameters of Standard Piezoelectric and Electrostrictive Materials .....	33
13. Perovskite Crystal Parameters for Traditionally Doped DoD Type I Materials.....	33
14. Room and Elevated Temperature Properties of Various DoD Type I Materials.....	37
15. Perovskite Crystal Parameters for Isovalently Doped DoD Type I Materials.....	37
16. Properties of Newly Developed Low T <sub>c</sub> Hard Piezoelectric Materials .....	38
17. Multilayer Piezoelectric Actuator Specifications and MSI Actuator Designs .....	41
18. Properties of MSI-53HD and PNN-1 Materials.....	41



## **1.0 Executive Summary**

The objective of this program was to utilize net shape injection molding forming processes to configure piezoelectric actuators to trade force for displacement in order to maximize performance and efficiency. The configurations were designed to gain mechanical advantage to increase the overall performance of the piezoelectric actuator system. The manufacturing approach also utilized low cost, reconfigurable tooling to enhance the flexibility of actuator fabrication.

The actuation requirements for a trailing edge helicopter rotorblade flap for Boeing Mesa's "Smart Materials Actuated Rotor Technology" program set the actuator performance goals towards which the program was directed. The ultimate goal required a large displacement, high energy density actuator, which would be expected to find use in a wide range of defense and commercial active vibration control and actuation applications. Materials Systems Inc. (MSI) was to attempt to design, fabricate, test, and deliver a piezoelectric actuator system to meet or exceed this challenging need.

In order to address these actuation requirements, MSI designed, fabricated, and tested several actuator systems. The first system was a volume actuator based on proven high  $d_h$  piezocomposite technology. Piezocomposite volume actuators offered ruggedness, volume efficiency, and easily redirected actuation direction. These actuators offered high displacement performance, particularly for applications that did not have stringent space or weight limitations. A subscale volume actuator was designed, built, and tested. Testing revealed limitations in performance due to low fluid bulk modulus and the need for a large pressure chamber. The large required volume resulted in actuation performance that met the displacement goal but at 23 times lower energy density than required.

Accordingly, the program was focused towards novel linear actuator approaches. A novel injection molded serpentine actuator element was developed. As a linear actuator, this new configuration exhibited free displacement increases of 10-fold over conventional  $d_{31}$  patch actuators and 4-fold over  $d_{33}$  multilayer devices. Various serpentine actuator configurations were designed, built, and tested. Initial stiffness data suggested that these actuators were capable of meeting the high strain and energy density requirements. However, actual force-displacement measurements showed that these actuators were capable of meeting the displacement requirements, but at 6 times lower energy density than required due to the lower than predicted stiffness.

In order to increase displacement and maintain a high energy density, an internally amplified multilayer actuator was designed and modeled. This actuator used low profile flexensional layers interspersed with multilayer piezoelectric actuator sections in order to have  $d_{31}$  actuation contribute with the standard  $d_{33}$  actuation. The best configurations were slightly low in both displacement and force. The energy density for the stainless steel design was 2 times lower than the requirement, whereas the aluminum design was 7 times lower than the requirement.

To utilize the various mechanical amplification schemes developed under this program, new high energy density piezoelectric materials were modeled, developed and examined. As part of this effort, MSI's high performance MSI-53HD and PNN-1 materials were configured into and tested as stacked co-fired multilayer actuators. In addition, research was initiated into piezoelectric ceramic

material combining qualities of both the hard and soft PZT-based materials. The new material was a low Curie temperature (240°C) DoD-I type material. By lowering the Curie temperature, high dielectric and piezoelectric properties were achieved, without significant sacrifice of the high drive properties. This material showed the potential for 1.7 and 2.8 times improvement in microstrain and energy density, respectively, over standard piezoelectric ceramics, including MSI-53HD material. Assuming that the field limit of the new material was correctly estimated, an internally amplified multilayer actuator produced using this new high energy density material has the highest potential at present for meeting the program actuation requirements. This ceramic material is now ready for configuration into multilayer actuator stacks for use in application demonstrations. Actual stack fabrication and performance demonstrations are proposed as a follow-on to this completed program.

Based on recent modeling results and data generated in this program, the best piezoelectric materials that have potential to meet the full range of helicopter rotorblade flap actuation requirements are the new class of "single crystal" PMN and PZN materials. The performance of these materials has only been demonstrated in single crystals grown by the expensive and shape-limited flux method. The application of these materials into helicopter rotorblades requires the development of a cost-effective single crystal multilayer manufacturing process, which is ongoing in other DARPA-funded programs. Upon successful demonstration of these advanced actuator materials in multilayer form, the logical next step would be to construct and evaluate full actuator stacks using tests developed under this program at MSI and at Boeing using rotorblade simulation equipment.

## **2.0 Program Objectives**

The objectives of this program were to design, fabricate, and characterize piezoelectric actuators tailored to meet the actuation requirements for a trailing edge helicopter rotorblade flap for the Boeing Mesa (formerly McDonnell Douglas Helicopter Company) "Smart Materials Actuated Rotor Technology" (SMART) program. The objective of the SMART program was to demonstrate smart materials for active control of helicopter rotorblade, using a piezoelectric actuator driven trailing edge flap for noise and vibration control and a shape memory alloy driven trailing edge trim tab for in-flight blade tracking. Boeing designed both the trailing edge flap and trim tab for the MD900 Explorer helicopter shown in Figure 1. The MD900 is a bearingless 5-bladed DoD-size utility aircraft weighing 6500 pound and capable of 155 knot flight speed. Since this helicopter has the widest noise compliance of all helicopters certified to date with an 83 dB FAR 36-H flyover noise level, it was an ideal test bed.

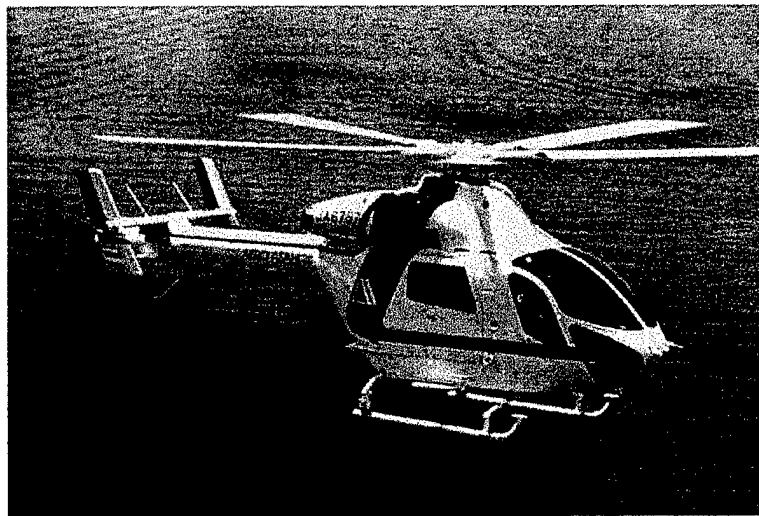


Figure 1. Boeing MD900 Explorer.

Figure 2 shows both the trailing edge flap and trim tab on the MD900 Explorer rotorblade. The goal for the trailing edge flap was the active reduction of noise and vibration. The active control flap was designed to provide a 10 dB reduction in blade vortex interaction (BVI) noise while landing, reducing detectability, and increasing community acceptance. The flap was also designed to reduce airframe vibrations by 80%, thereby improving ride quality and component reliability and life.

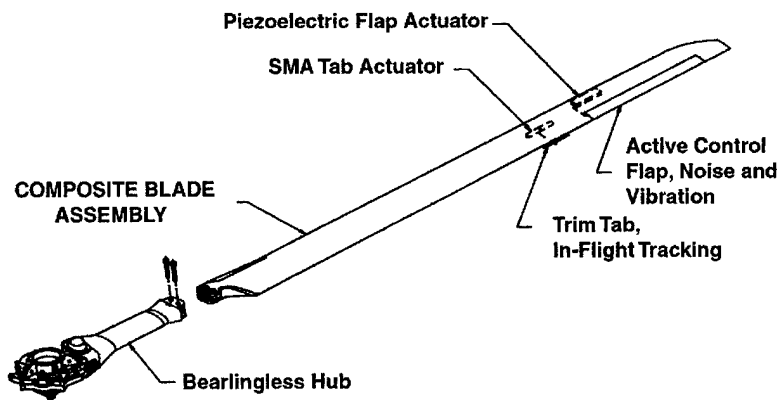


Figure 2. MD900 Explorer rotorblade with integral trailing edge flap and trim tab.

As shown in Figure 3, the actuator for the trailing edge flap was designed to be integral to the rotorblade. This design allows for minimal impact on blade structural integrity. Its modular design allows for ease of changing actuators, testing alternate piezoelectric actuator designs, maintainability, and serviceability. The design also minimizes the actuation requirements to only aerodynamic loading from the flap deflection, without additional airfoil contour actuation. However, since the actuator must physically fit within a small section of the blade and must have its center of mass forward of the blade's center of mass, the actuator energy density must be very high.

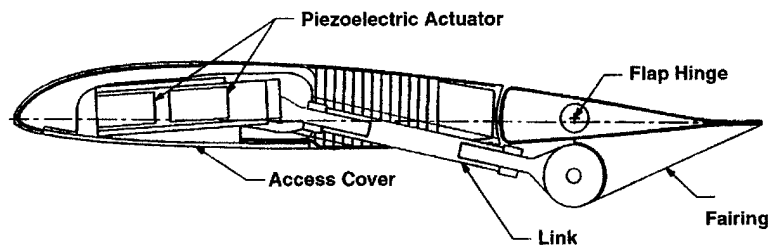


Figure 3. MD900 Explorer HH10 airfoil cross-section showing the forward location of the piezoelectric actuator.

The trailing edge flap requires a large displacement, high energy density piezoelectric actuator, due to its relatively high frequency, high energy density, and wide bandwidth requirements. The specific actuator requirements are shown in Table 1. Compared with state-of-the-art multilayer piezoelectric actuators, the rotorblade flap actuator requires thirteen times the strain capability at 55% of the total energy available.

**Table 1. Boeing Actuation Requirements**

ITEM	REQUIREMENT
Displacement	$0.000 \pm 1.473$ mm
Load	$285 \pm 215$ N
Frequency	39.2 Hz
Phase Lag	$\leq 10$ degrees
Temperature Range	-50 to 70°C
<u>Acceleration Environment</u>	
Radial	665 g
Thickness	90 g
Chordwise	25 g
Length	$\leq 305$ mm
Weight	$\leq 1.8$ kg
Center of Gravity	$\leq 63.5$ mm from leading edge
Actuator Life	>4500 hours ( $635 \times 10^6$ cycles)
Attachment to Flap	chordwise

### **3.0 Technical Approach**

The principal technical approach to resolving this actuator problem was to utilize net shape injection molding forming processes for configuring piezoelectric actuators that trade force for displacement in order to maximize performance and efficiency. The configurations were designed to increase mechanical advantage and thereby improve the overall performance of the actuator. The piezoelectric ceramic forming approaches utilized low cost, reconfigurable tooling to enhance the flexibility of actuator fabrication.

Several approaches were possible for meeting the high displacement, high energy density rotorblade flap actuation requirements. One approach used a very efficient mechanical amplification system to increase the displacement capability without significantly reducing the energy density. Another approach utilized a high energy density actuator material in various amplification schemes. Both approaches were investigated during this program.

Displacement amplification was accomplished by various means, including hydraulics, serpentine actuation, and flextensional amplification. Hydraulic amplification was used with a volume actuator design based on MSI's high  $d_h$  piezocomposite technology. Piezocomposite volume actuators offered ruggedness, volume efficiency, easily redirected actuation direction, and utilization of proven piezocomposite technology.

The second mechanical amplification approach utilized a new family of linear piezoelectric actuators that offered a wide range of force-displacement characteristics. These serpentine actuators achieved high strain capability via mechanical amplification within the actuator structure.

Since co-fired multilayer actuators could meet the energy density requirements, an internally amplified multilayer configuration was examined to increase the displacement and maintain the required energy density. The internal amplification was accomplished with flextensional layers interspersed with multilayer sections in order to use the  $d_{31}$  motion of the actuator in conjunction with the  $d_{33}$  motion.

All of the mechanical strain amplification systems examined had limited force-displacement conversion efficiencies. For any of these schemes to meet the actuation requirements, more energy must be delivered from the piezoelectric material. Therefore, high energy density piezoelectric materials were examined. The materials included a high performance DoD Type VI soft PZT (MSI-53HD), a high performance PNN (PNN-1), and a new high performance modified DoD Type I material.

## 4.0 Results

### 4.1 1-3 Piezocomposite Volume Actuator

MSI designed, fabricated, and tested a subscale volume actuator (shown in Figures 4-6). A total of thirty-four 50 volume percent DoD-VI 1-3 piezocomposite elements were stacked to form a 50 mm long actuator. The volume actuator was placed into the pressure vessel as shown in Figure 7. Figures 8 and 9 show photographs of the volume actuator and pressure vessel.

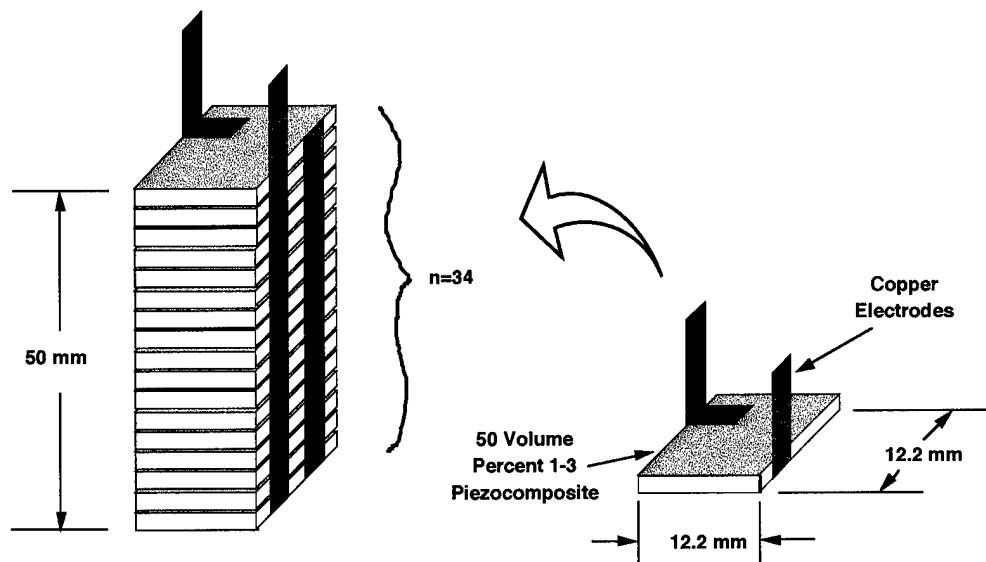


Figure 4. Subscale volume actuator fabricated from thirty-four 50 volume percent DoD-VI 1-3 piezocomposite elements.

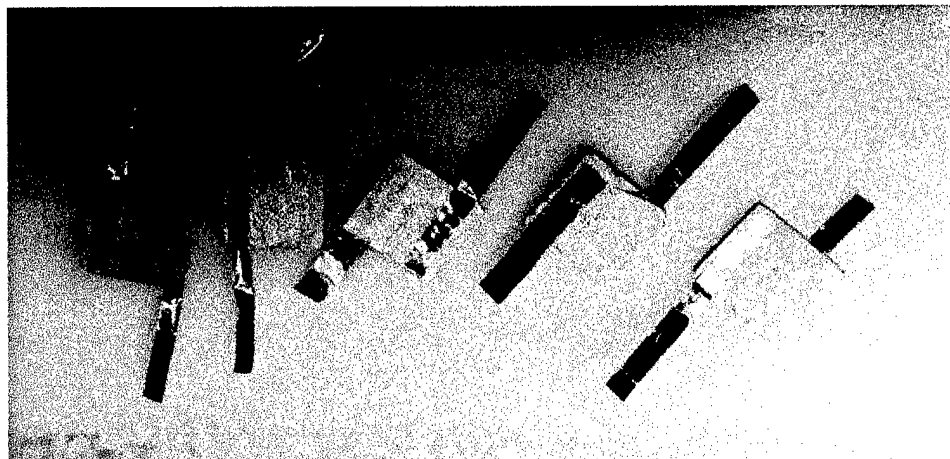


Figure 5. Individual 50 volume percent DoD-VI 1-3 piezocomposite elements showing silver epoxy electrodes and copper interconnect tabs.

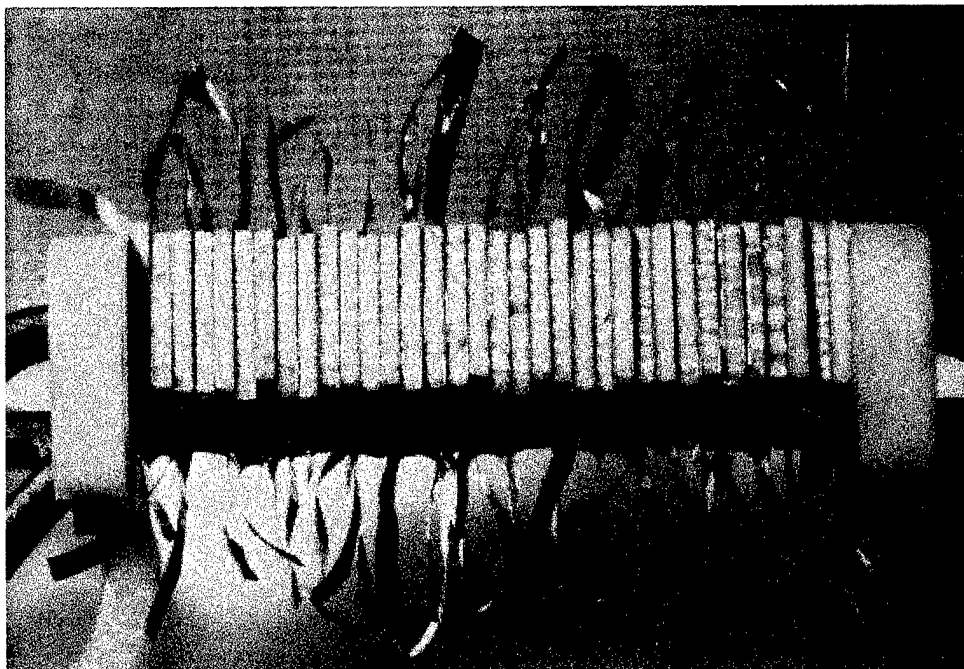


Figure 6. Thirty-four 1-3 piezocomposite elements were stacked to form the volume actuator.

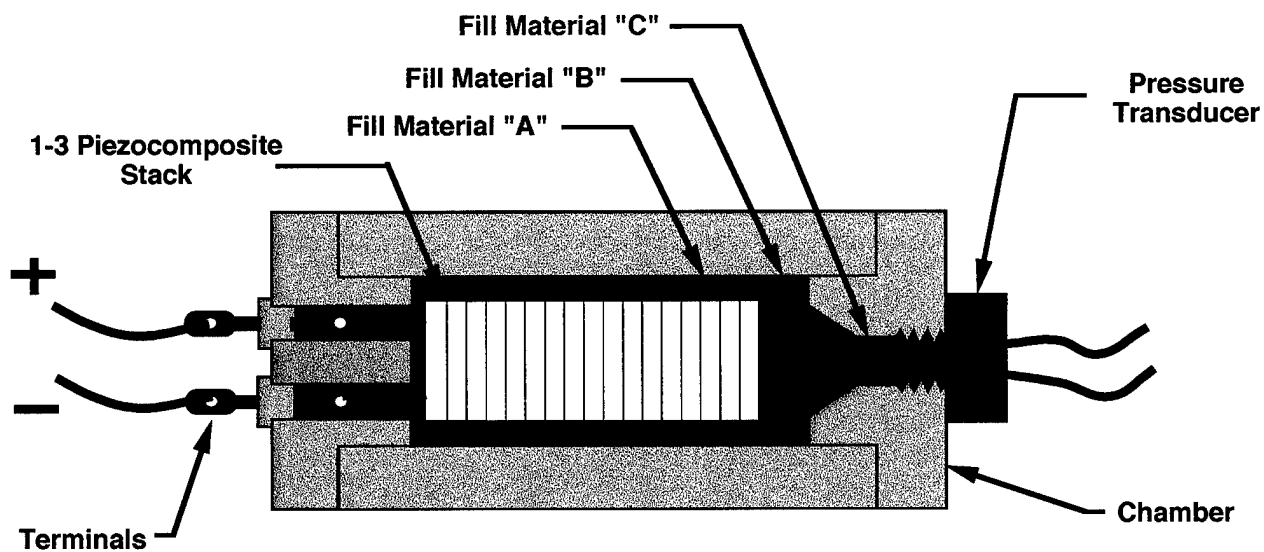


Figure 7. Schematic of the volume actuator located within the pressure vessel. Fill materials A, B, and C are described in Table 2.



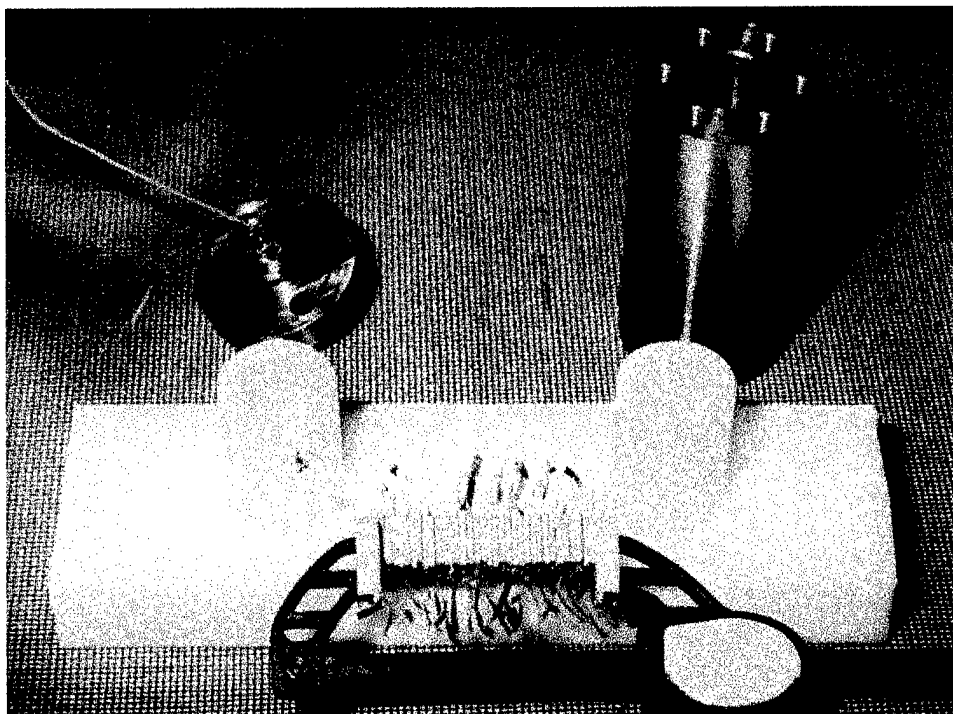


Figure 8. Volume actuator and pressure vessel prior to assembly.

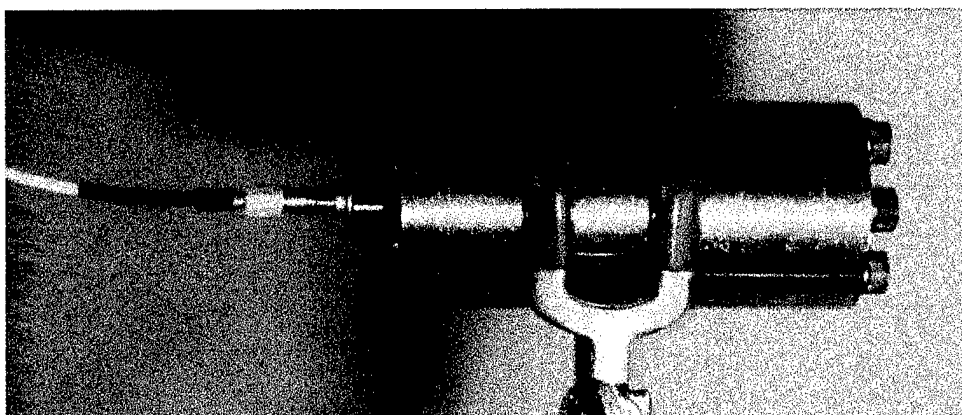


Figure 9. Volume actuator sealed in pressure vessel for constrained pressure measurements at 45 Hz.

In order to measure the free displacement, the vessel was filled with dielectric fluid, and a transparent 0.635 mm diameter tube was inserted into the pressure transducer port. This allowed the fluid level to be measured. Up to 400V<sub>DC</sub> was applied to the volume actuator. Figure 10 summarizes the unconstrained actuator test results.

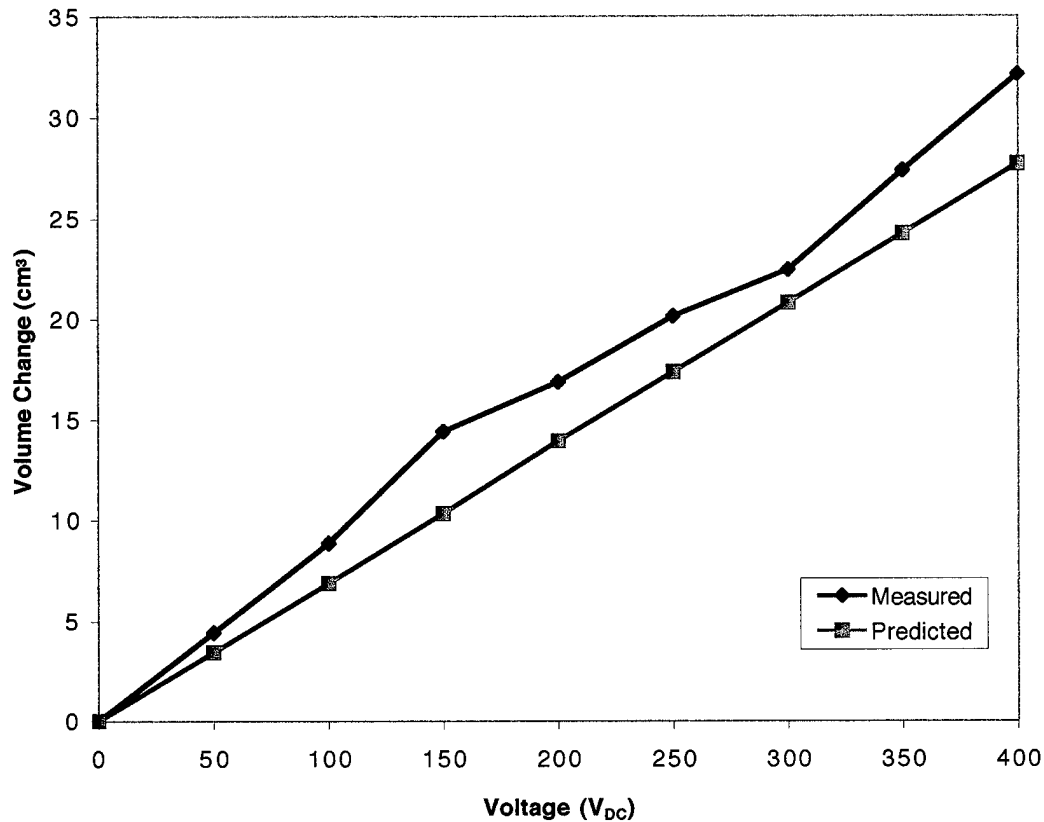


Figure 10. Static volume change of unconstrained actuator.

The volume actuator was then sealed to measure the output pressure using various fill materials. Table 2 describes the three test cases.

**Table 2. Summary of Test Cases**

TEST CASE NO.	FILL MATERIAL		
	"A"	"B"	"C"
1	Dielectric Fluid	Dielectric Fluid	Dielectric Fluid
2	Shore D 80 PU	Shore A 65 PU	Dielectric Fluid
3	Shore D 80 PU	Shore A 65 PU	Shore A 65 PU

Figure 11 summarizes the test results for the constrained actuator at 45 Hz. The bulk modulus of an elastomer which is similar to Shore A 65 Polyurethane (6.9 GPa) was used to make a rough estimate of the pressure increase based on the free displacement. The Case 3 data shows that the actuator developed more pressure than predicted, indicating that the elastomer was reasonably stiff and free from voids.

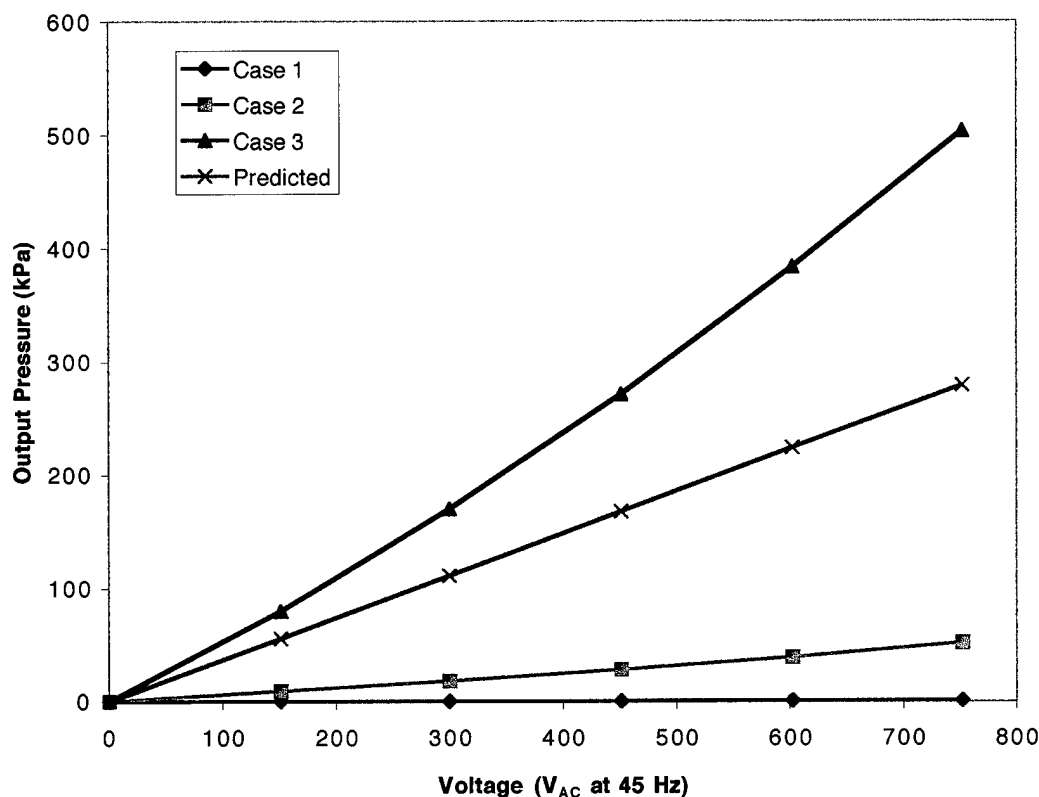


Figure 11. Output pressure from a constrained volume actuator at 45 Hz for three different fill test cases versus the predicted filler with for a 6.9 GPa bulk modulus.

Based on the proof-of-principle data shown in Figures 10 and 11, a full scale actuator (305 mm long) would provide 2.946 mm peak-to-peak displacement if the piston diameter were 0.914 mm. Since the maximum pressure at 296 kV/m was 503 kPa, this would result in a 0.33 N blocked force, which is insufficient for the helicopter application even after scaling factors are taken into account. Several improvements could increase the blocked force without reducing the displacement. These are shown in Table 3. If all of these improvements were accomplished, the blocked force would increase to approximately 18 N. However, this is 23 times lower than the minimum blocked force of 427 N required to meet the requirements shown in Table 1.

**Table 3. Potential Improvements to Volume Actuator**

IMPROVEMENT	FORCE INCREASE (est.)
Reduced Fluid Volume	5 x
Increased Bulk Modulus	3.5 x
Increased Voltage (1 MV/m)	3.2 x
Total	56 x

Higher energies could be obtained at resonance. Figure 12 shows the resonance behavior of the nearly unconstrained case 1 volume actuator. However, the full-scale actuator would have too high resonance frequency (~1800 Hz) and too low bandwidth to fulfill the actuation requirements.

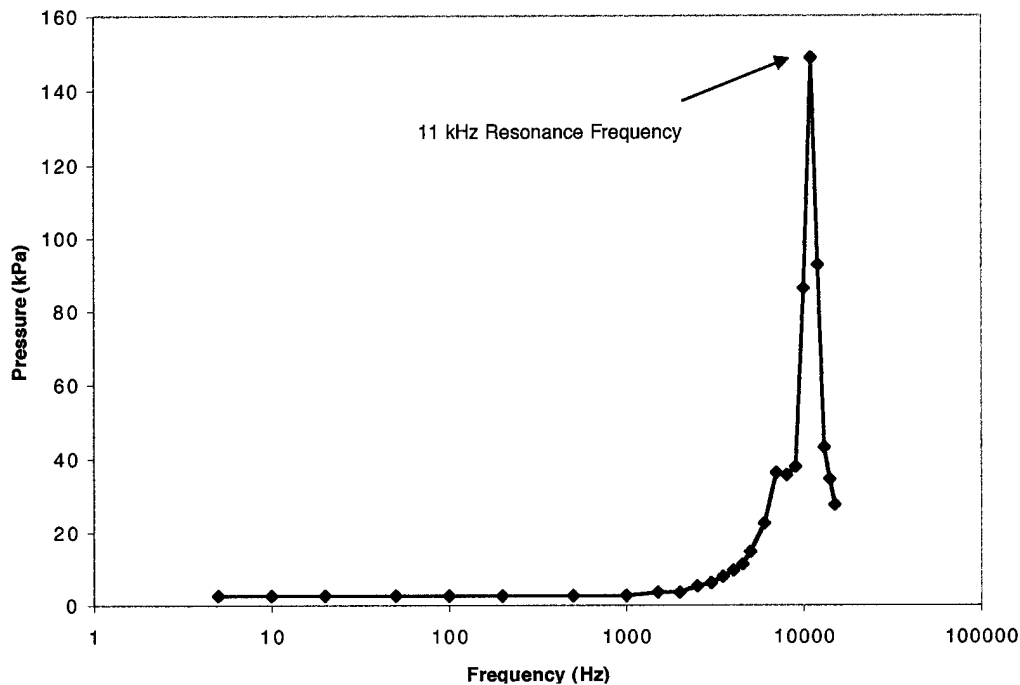


Figure 12. Frequency response of the nearly unconstrained case 1 volume actuator, showing an 11 kHz resonance.

In view of the apparent limitations of volume actuation using force transfer via hydraulic fluid, this approach was abandoned after completing the subscale technical demonstration. Useful actuator performance was obtained for several alternative applications, such as lower energy density actuators and piezoelectric pumps. However, this method proved unsuitable for use in helicopter rotorblade actuation.

## 4.2 Serpentine Element-Driven Linear Actuator

### 4.2.1 Serpentine Actuator Design

Based on initial displacement results for a new injection molded serpentine actuator element developed under a previous NASA program (Contract No. NAS1-20626), MSI refocused most of the actuator development activity onto the development and incorporation of serpentine actuator elements for use in a linear actuator. A schematic representation of the serpentine actuator is shown in Figure 13. These actuators had a thin cross section, allowing them to be used for surface mounted, embedded, or bender applications. The actuators were fabricated by injection molding and electroded by electroless nickel plating, both low-cost manufacturing techniques. A cross-section of a serpentine actuator is shown in Figure 14.

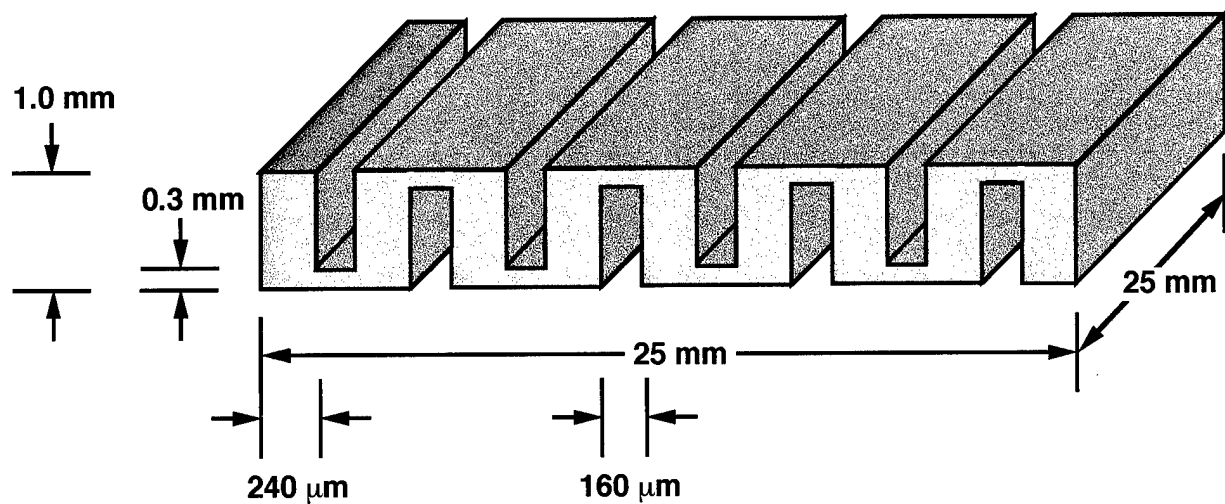


Figure 13. Schematic representation of serpentine PZT actuator showing typical dimensions.

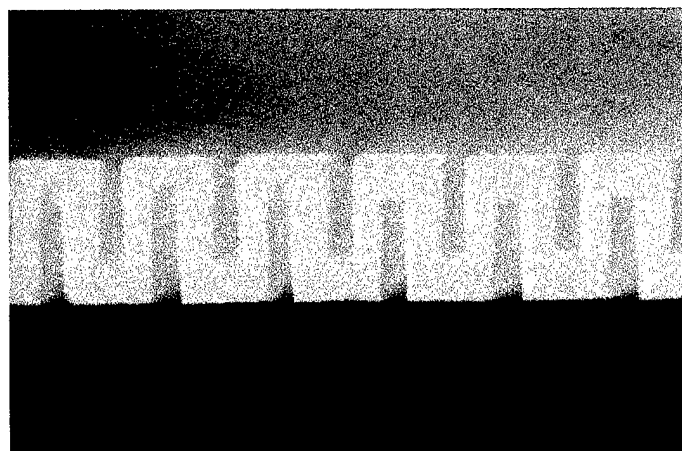


Figure 14. As-fired serpentine actuator fabricated by injection molding. Serpentine actuator has ~240 μm PZT layers and ~160 μm gaps.

Serpentine actuator elements were designed to be stacked in a hollow, "brickwork" structure to form a linear actuator. A 15 x 22 x 127 mm quarter scale stack is shown in Figure 15. The design required approximately 200 serpentine actuator elements built into a "brickwork" stack to increase buckling strength. Space was left to pass the tension rod through the center of the stack. Kynar film and alumina plates provided the insulation from the center rod and end plates. A threaded rod, a nut, and a Belleville spring were used to preload the stacks to maintain compression. Figure 16 shows the complete linear actuator configuration.

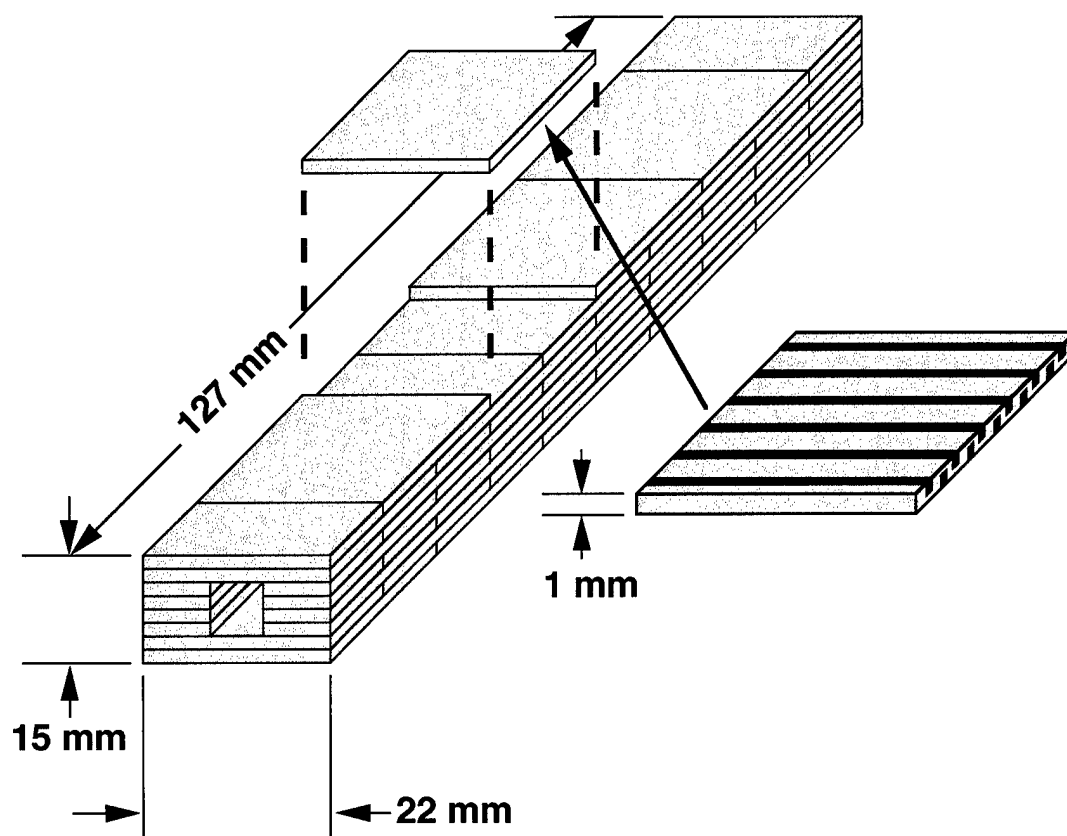


Figure 15. Serpentine actuator elements are stacked to form a brickwork structure to increase buckling strength. Space is left to pass the tension rod through the center of the stack.

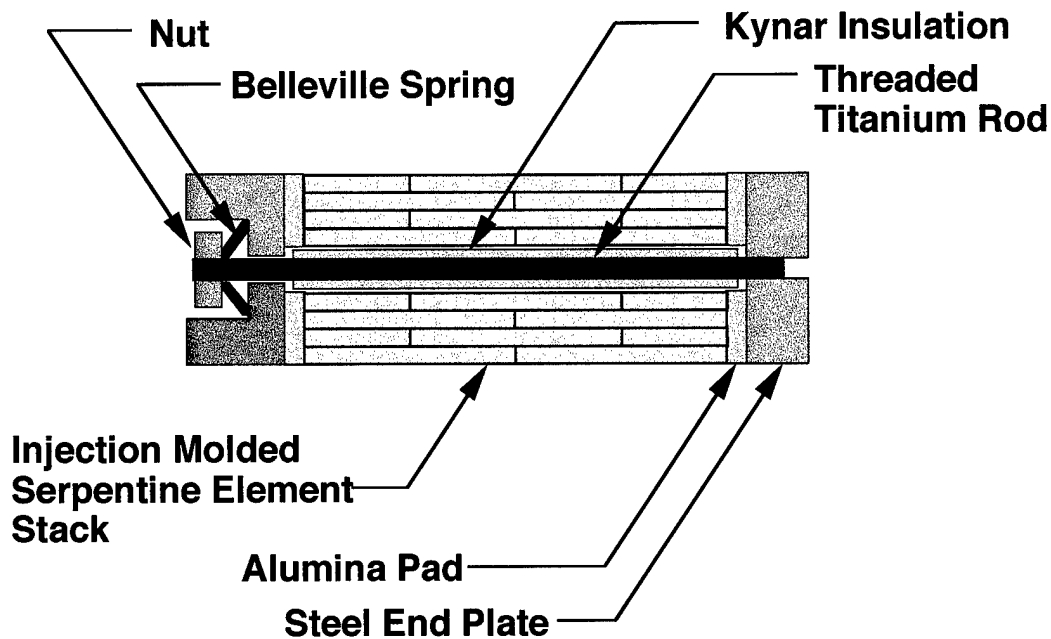


Figure 16. The linear serpentine-driven actuator was designed to use a Belleville spring to maintain a compressive preload and Kynar film and alumina plates to provide electrical insulation from the center rod and end plates.

The serpentine-driven linear actuator was designed for use with a limited mechanical amplification to increase displacement (Figure 17). The design placed serpentine stacks on either side of a flexure element to reduce bending loads and facilitate installation. The mechanical amplifier design reduced the load by a factor of 3.4 in order to achieve the predicted 2.9 mm free displacement and 77 N blocked force. The amplifier also provided a mechanism for converting the output from the radial to chordwise direction.

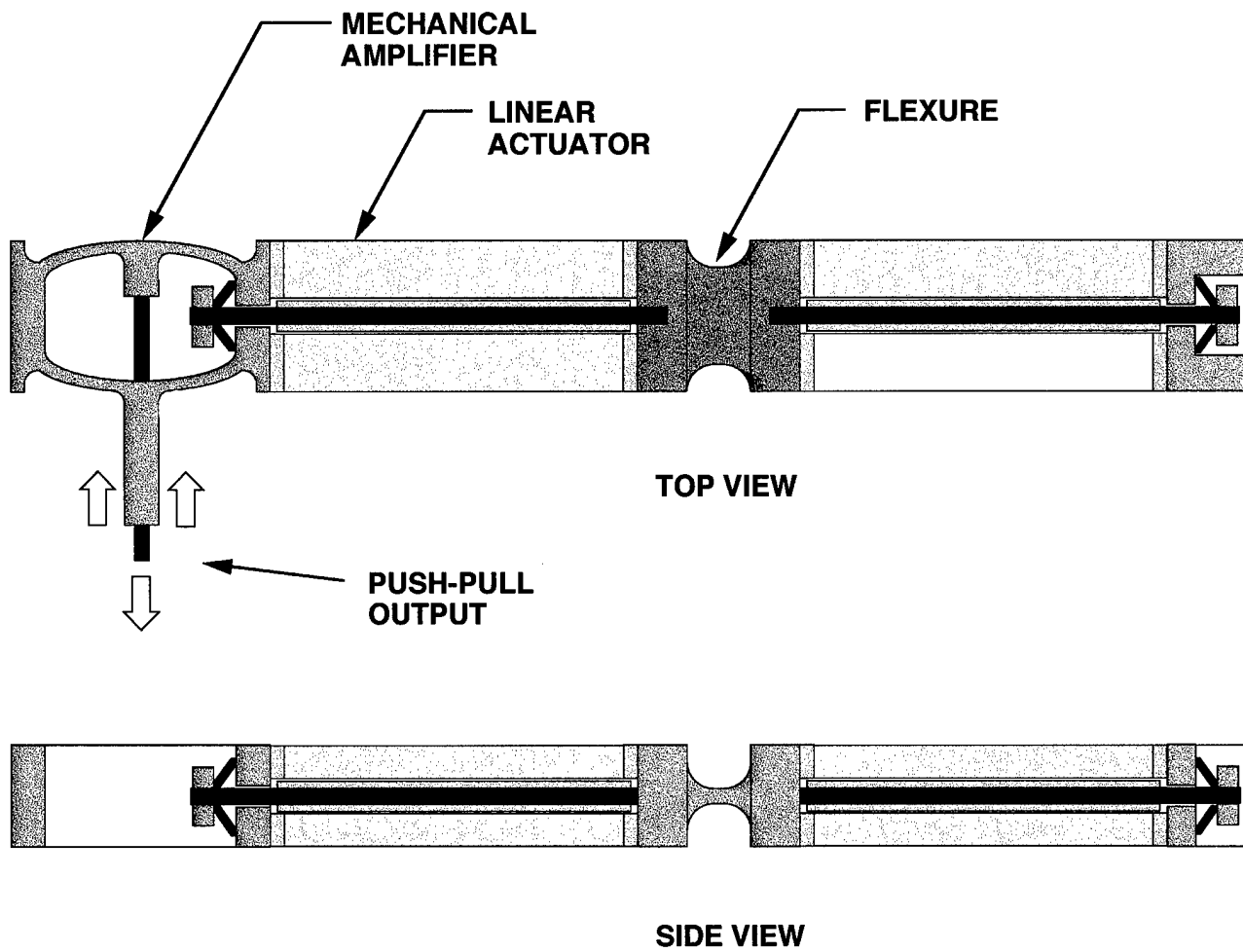


Figure 17. Amplified serpentine-driven linear actuator with 3.4:1 flextensional mechanical amplifier.



#### 4.2.2 Serpentine Elements

The serpentine actuator elements were fabricated by injection molding. A schematic of the fabrication technique and tool design is shown in Figure 18. Piezoelectric ceramic powder was mixed with a wax-based binder. This mixture was heated and injected under pressure into a cold metal mold, and ejected to form a green part. This green part then underwent binder burnout and sintering to produce the final net shape. For a  $d_{33}$ -polarized element, the fired part was plated with electroless nickel, trimmed to size, and then polarized. For a  $d_{15}$ -polarized element, the fired part was polarized, plated with electroless nickel, and then trimmed to size. After testing, the elements were assembled as an actuator stack. In order to adapt and scale the processing of serpentine actuators to the helicopter rotorblade actuator application, MSI fabricated over 200 DoD-VI serpentine actuators.

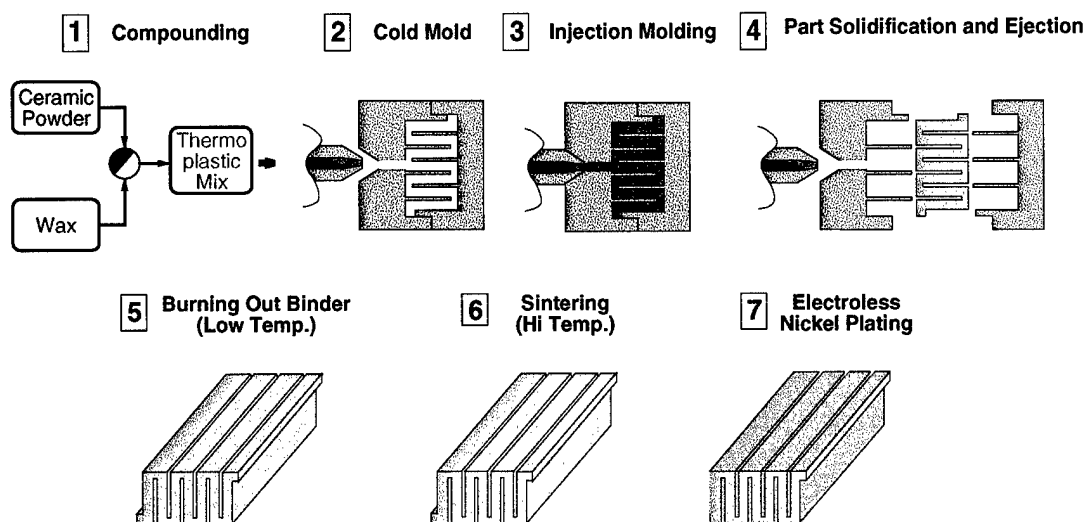


Figure 18. Schematic description of the injection molding, firing, and electroding processes for serpentine element fabrication.

Tooling modifications were required to refine tool alignment and to eliminate geometrical variations. Tooling was fabricated with chamfered inside corners to minimize processing and operational defects, such as pin holes, longitudinal cracks, incomplete part formation, and dimensional variations.

In addition to material processing, molding conditions were extensively evaluated and optimized. Molding conditions included temperature, pressure, heat up rate, cool down rate, pressurization rate, and dwell times. These studies were required to eliminate material defects and improve dimensional consistency.

Early small scale serpentine actuators were electroded with either in-house sputtered Ti/Au and Cr/Au or out-of-house electroless nickel plating. A surface treatment condition was developed to improve the adhesion of all of these electrode types. Due to inconsistent quality of the nickel

plating from outside vendors, the electroless nickel plating process was brought in-house. The nickel plating was evaluated by extent of coverage, adhesion, penetration into the actuator gaps, and plating resistance. It was found that the in-house electroless nickel plating with no surface pretreatment produced the most complete electrode coverage; all other electroding techniques resulted in incomplete electrode coverage. The in-house electroless nickel process was then optimized by making refinements to the cleaning, sensitizing, activation, plating, and various rinse steps. Refinements included time, temperature, and bath chemistry. The optimized nickel plating process gave complete coverage with an electrode resistivity of  $\sim 12.5 \Omega\text{-cm}$ .

Both  $d_{33}$  and  $d_{15}$  serpentine actuators were produced and tested. Table 4 compares the effective  $d_{ij}$  and free longitudinal displacements of standard  $d_{31}$  plates, standard  $d_{33}$  multilayer,  $d_{33}$ -polarized unfilled serpentine, and  $d_{15}$ -polarized unfilled serpentine actuators. Both serpentine actuator configurations show significant improvements in free displacement. All actuators were  $25 \times 25 \times 1$  mm in size and tested at  $140 V_{pp}$  at 80 Hz.

**Table 4. Actuation Displacement Performance Comparison between  $d_{31}$  Plate,  $d_{33}$  Multilayer, and Two Serpentine Actuator Configurations**  
( $25 \times 25 \times 1$  mm Actuator Tested at  $140 V_{pp}$  at 80 Hz).

Actuator Description	Effective $d_{ij}$ ( $10^{-12}$ m/V)	Free Longitudinal Displacement ( $\mu\text{m}$ )
standard $d_{31}$ plate	274	1.5
monolithic $d_{33}$ multilayer	593	8.4
$d_{33}$ -polarized serpentine	1446	20.4
$d_{15}$ -polarized serpentine	2440	34.2

Serpentine actuators were produced both unfilled and filled with various polymer materials. The use of fillers was investigated as a means to improve buckling strength without seriously impacting actuation performance. Each candidate fill material was cast into tensile test specimens and tested for room temperature strength and dynamic mechanical properties over a range of temperatures. Table 5 shows some average tensile properties for three test samples of each candidate material. All fill materials appeared to have suitable elongation properties to accommodate serpentine actuation strain.

**Table 5. Average Tensile Properties of Candidate Fill and Encapsulant Materials**

Material	Strength (MPa)	0.2% Yield Strength (MPa)	% Elongation
Hard Fill	48.0	36.5	3.9
Semi-Hard Fill	5.8	0.8	59.8
Semi-Soft Fill	4.4	0.4	71.3
Soft Fill	0.6	0.3	18.1

Serpentine actuator displacements were measured and compared under both free and loaded (3.1, 6.2, and 12.4 MPa) conditions at frequencies from 10 Hz to 1 kHz. Table 6 shows the actuator limits and operating conditions for a 12.5 x 12.5 x 1.0 mm  $d_{33}$ -polarized DOD-VI serpentine element, tested at 140 V<sub>pp</sub>. The data show that the harder the filler material, the higher the preload that the actuator can withstand. Both the semi-soft and hard filled serpentine could meet the required loading conditions. Figure 19 shows the force versus displacement test results for both medium filled and unfilled 25 x 25 x 1.0 mm samples polarized in the  $d_{15}$  condition and tested at 140 V<sub>pp</sub>. These data show that the free displacement is significantly reduced with the filler material, whereas the blocked force was not affected. Therefore, the use of fill material improves actuator ruggedness at the expense of both actuator free displacement and energy density.

**Table 6. Actuator Limits and Compressional Operating Conditions for 12.5 x 12.5 x 1.0 mm  $d_{33}$ -Polarized Serpentine Element at 140 V<sub>pp</sub>**

Property	Fill Material		
	Soft	Semi-Soft	Hard
Free Displacement ( $\mu\text{m}$ )	11.2	5.4	1.5
Effective $d_{33}$ ( $\times 10^{-12}$ m/V)	1440	696	189
Maximum Preload (N)	8	71	165
Maximum Blocked Pressure (MPa)	0.6	5.6	12.9

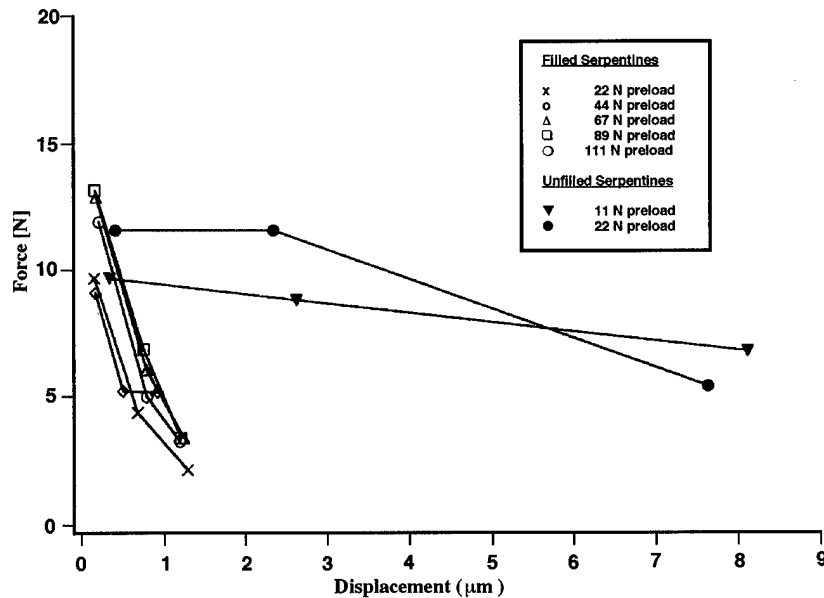


Figure 19. Force versus displacement characteristics of medium-filled and unfilled  $d_{15}$ -polarized 25 x 25 x 1 mm serpentine actuator tested at 140 V<sub>pp</sub> at 40 Hz.

As shown from the force-displacement results, the high free displacement and maximum strain performance of serpentine actuator elements was achieved at the expense of both block force and energy density. Table 7 compares the maximum strain, blocked force, energy, and energy density of standard  $d_{31}$  plates, standard  $d_{33}$  multilayer,  $d_{33}$ -polarized unfilled serpentine, and  $d_{15}$ -polarized unfilled serpentine actuators. All actuators were 25 x 25 x 1 mm in size, were manufactured with DoD VI material, and were tested at 2 MV/m. The reason for the lower energy output was the uneven field and stress distributions in the serpentine structure, where those areas of high tensile stress detract from the actuation performance. The even field and stress distributions in the standard  $d_{31}$  plates and standard  $d_{33}$  multilayer designs allowed all of the material to contribute to the actuation performance.

**Table 7. Actuation Performance Comparison between Standard  $d_{31}$  Plates, Standard  $d_{33}$  Multilayer, and Two Serpentine Actuator Configurations**  
(25 x 25 x 1 mm Actuator Tested at 2 MV/m).

Actuator Description	Maximum Strain ( $\mu\epsilon$ )	Blocked Force (N)	Energy (mJ)	Energy Density ( $\text{kJ/m}^3$ )
standard $d_{31}$ patch	548	930	3.5	5.7
monolithic $d_{33}$ multilayer	1186	1440	11.0	17.6
$d_{33}$ -polarized serpentine	2892	18.4	0.34	0.9
$d_{15}$ -polarized serpentine	4880	14.9	0.46	1.2

The serpentine actuators were thoroughly tested under both free and loaded conditions. Although the free displacement data and calculations showed these devices to have adequate properties for the helicopter rotorblade flap application, the loaded condition resulted in poor force generation characteristics.

As the work progressed, it became apparent that the original calculations of serpentine actuator performance, based on resonance stiffness data, did not adequately represent the measured loaded data. The problem appeared to be with the overestimated stiffness of serpentine geometries rather than a fundamental issue with the serpentine actuator or its fabrication. Accordingly, efforts were initiated with a modeling subcontractor, Weidlinger Associates, to better understand the behavior of the serpentine actuators. In conjunction with the modeling, a test rig was developed to allow actuator performance to be measured accurately under various dynamic loading conditions.

### 4.2.3 Serpentine Element Modeling

To determine if the measured force-displacement characteristics of the serpentine actuator were due to the device structure or to its fabrication, the serpentine actuator structure was modeled using PZFlex code (version 1-H.5, Weidlinger Associates) by an explicit time-domain finite element technique. The key results of this analysis are summarized below. Figure 20 shows an example of the modeling results for an unfilled  $d_{33}$ -polarized serpentine element. Though the modeling showed slightly lower free displacement and slightly higher block force than measured results, it confirmed that the actuation performance was due to the serpentine structure, rather than its materials or fabrication methods. Table 8 compares the measured with the modeled free longitudinal displacements for 25 x 25 x 1 mm serpentine actuator at 140 V<sub>pp</sub>. Finite element analysis confirmed that the  $d_{15}$  configuration has higher free displacement. Modeling also showed a high sensitivity of free displacement to inactive layer thickness, but no sensitivity to electrode coverage at the bottom of the gap.

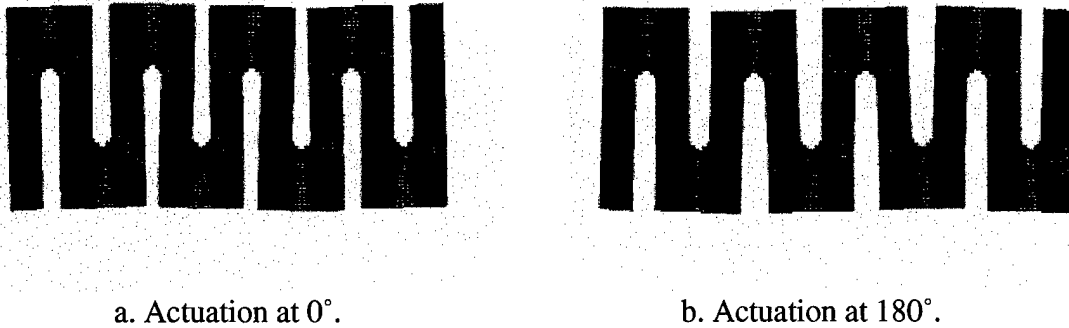


Figure 20. Modeling results for an unfilled  $d_{33}$ -polarized serpentine element.

**Table 8. Summary of Measured and Modeled Longitudinal Displacements**  
(25 mm long unfilled serpentine actuator at 140 V<sub>pp</sub> at 80 Hz)

Description	Measured Displacement	Modeled Displacement
Solid $d_{31}$ plate	1.5 $\mu\text{m}$	1.5 $\mu\text{m}$
Solid $d_{33}$ multilayer	8.3 $\mu\text{m}$	9.0 $\mu\text{m}$
$d_{33}$ -polarized serpentine (nominal dimensions)	20.4 $\mu\text{m}$ (unfilled) 4.1 $\mu\text{m}$ (filled)	8.9 $\mu\text{m}$
$d_{33}$ -polarized serpentine (thin inactive 0.15 mm)	0.5 $\mu\text{m}$	21.7 $\mu\text{m}$
$d_{33}$ -polarized serpentine (no electrode in gap bottom)	1.2 $\mu\text{m}$	8.7 $\mu\text{m}$
$d_{15}$ -polarized serpentine (alt. direction)	1.7 $\mu\text{m}$	1.2 $\mu\text{m}$
$d_{15}$ -polarized serpentine (one direction)	34.2 $\mu\text{m}$	10.3 $\mu\text{m}$

In order to increase the force output and energy density of the serpentine actuators, various actuator geometric configurations (gap overlaps) were modeled. Table 9 shows a comparison of the modeled versus actual performance of several actuator configurations. The modeling indicated that blocked force changes only modestly with actuator gap overlap. The maximum work obtainable increases with increasing gap overlap.

**Table 9. Comparison between Actual and Modeled 25 x 25 x 1 mm  $d_{15}$ -Polarized Serpentine Actuator Performance for Various Gap Overlaps at 140 V<sub>pp</sub>**

Actuator Configuration	Free Displacement ( $\mu\text{m}$ )		Blocked Force (N)		Maximum Energy (J)	
	Actual	Modeled	Actual	Modeled	Actual	Modeled
Full overlap	34.2	22.8	4.1	9.2	35	52
Half overlap	13.1	11.5		10.0		29
Third overlap	5.6	2.2		11.2		6.2

#### **4.2.4 Serpentine Element Testing**

MSI designed and built the actuator test facility shown in Figure 21 to evaluate the serpentine actuator elements and the stack linear actuator performance under dynamic or spring loads. The apparatus allowed the spring load and impedance to be changed. A load cell was used to monitor the static preload, a force sensor was used to monitor the magnitude and phase of the dynamic loads, and a photonic sensor was used to measure displacement. The magnitude and phase of the voltage and current were also recorded, so that the entire "two in - two out" transfer function could be determined.

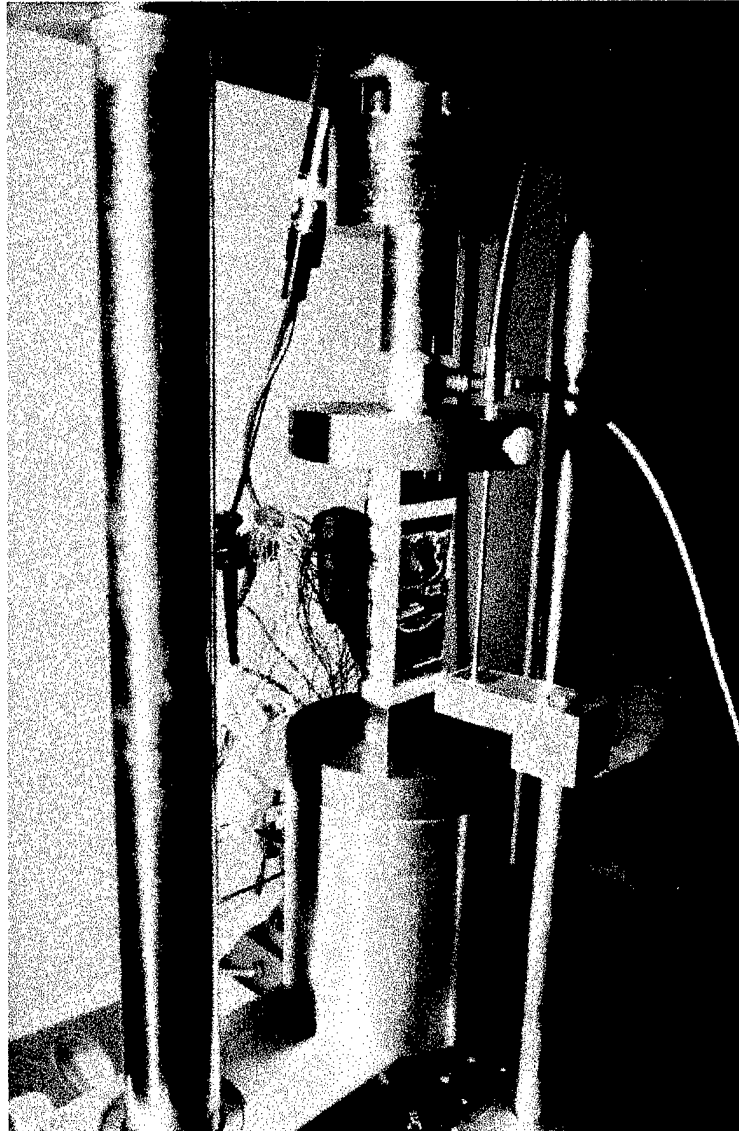


Figure 21. MSI actuator test facility which measures voltage, current, force, displacement and their phase relationships under various static loads, mechanical impedances, temperatures, and frequencies.

Using the test facility, 25 x 25 x 1 mm injection molded serpentine actuator elements were tested in both unfilled condition and filled with semi-hard polymer. Figure 22 shows an unfilled 25 x 25 x 1 mm  $d_{15}$ -polarized serpentine actuator element. In addition, three filled and unfilled elements were assembled in a 25 x 25 x 3 mm linear actuator shown in Figure 23. Figure 19 above shows force-displacement performance for both filled and unfilled 25 x 25 x 3 mm linear actuators at 140 V<sub>p-p</sub> at 40 Hz. While the use of fill materials improved the compression and bending strength of the actuator element, the force-displacement data showed that the use of fill materials degraded the displacement performance of the actuator element with no improvement in force capability. From this data, the full-scale linear actuator was predicted to provide 2.9 mm free displacement and 77 N blocked force or approximately 5.5 times lower energy density than the Boeing actuation requirement.

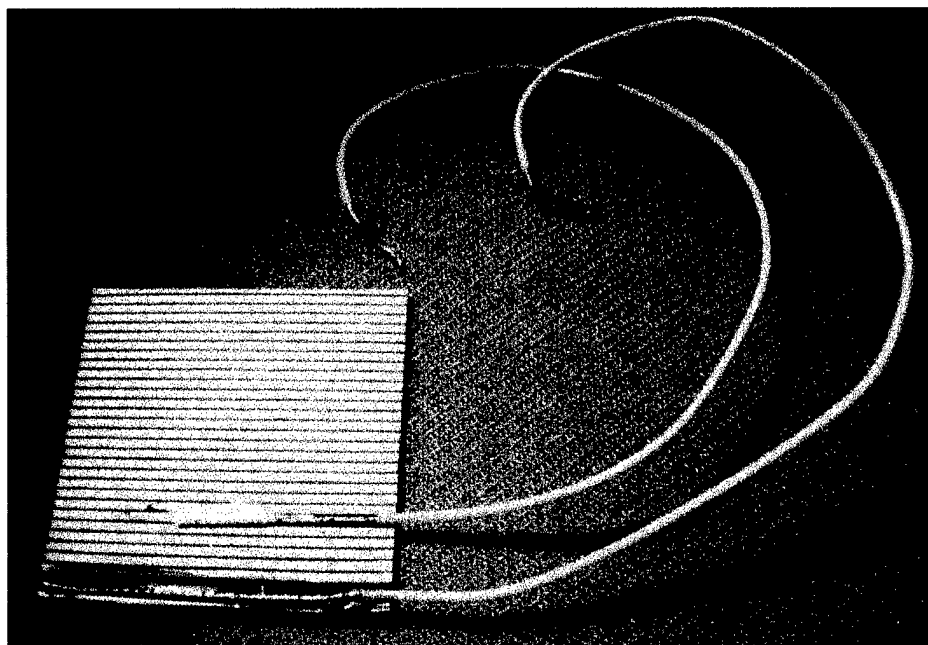


Figure 22. An unfilled 25 x 25 x 1 mm  $d_{15}$ -polarized serpentine actuator element.



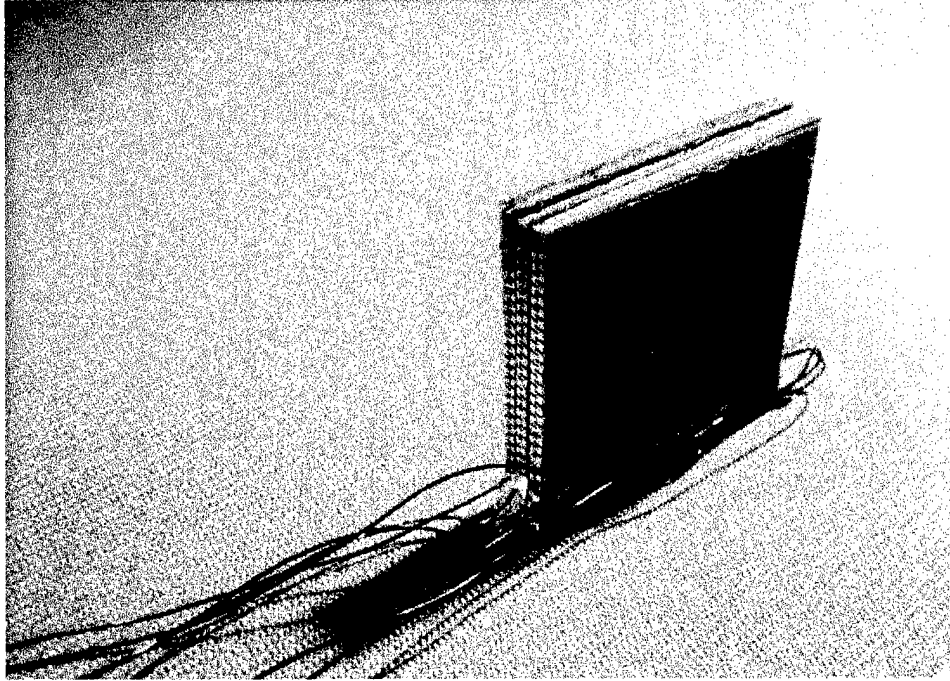


Figure 23. Serpentine actuator stack consisting of three 25 x 25 x 1 mm actuator elements.

The result of the serpentine actuator development was that the serpentine configuration allowed for high free displacement or strain capability at the expense of force generation and energy density. Although this trade-off is acceptable in certain applications, the low force generation precluded the use of serpentine-driven linear actuators in helicopter rotorblade actuation. In view of this result, the quarter scale linear actuator was not built or tested and the efforts were refocused onto internally strain-amplified designs.

### **4.3 Internally Amplified Multilayer Actuator**

As another approach to increasing displacement while maintaining a high energy density, MSI designed and characterized a linear multilayer actuator utilizing internal flextensional mechanical amplification. The internal amplification was designed to have the  $d_{31}$  actuation response contribute in concert with the  $d_{33}$  response. A schematic of the flextensional amplifier is shown in Figure 24. The mechanical amplifier consists of a low profile internal flextensional layer designs interspersed between layers of MSI-53HD multilayer piezoelectric actuators. Various flextensional layers were modeled using PZFlex. Modeling variables included material properties, curvature, layer thickness, and the use of flexure notches. The selected internal flextensional amplifier modeling cases are shown in Figure 25, with their corresponding results shown in Table 10. These cases are compared with the MSI-53HD material baseline.

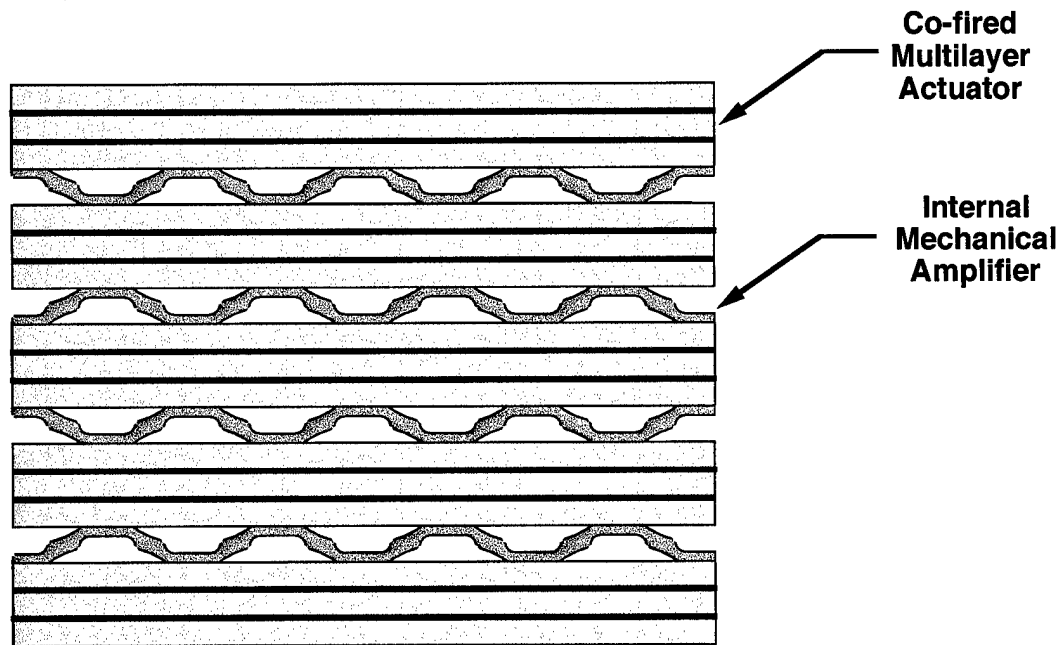


Figure 24. Schematic of internally amplified multilayer actuator.

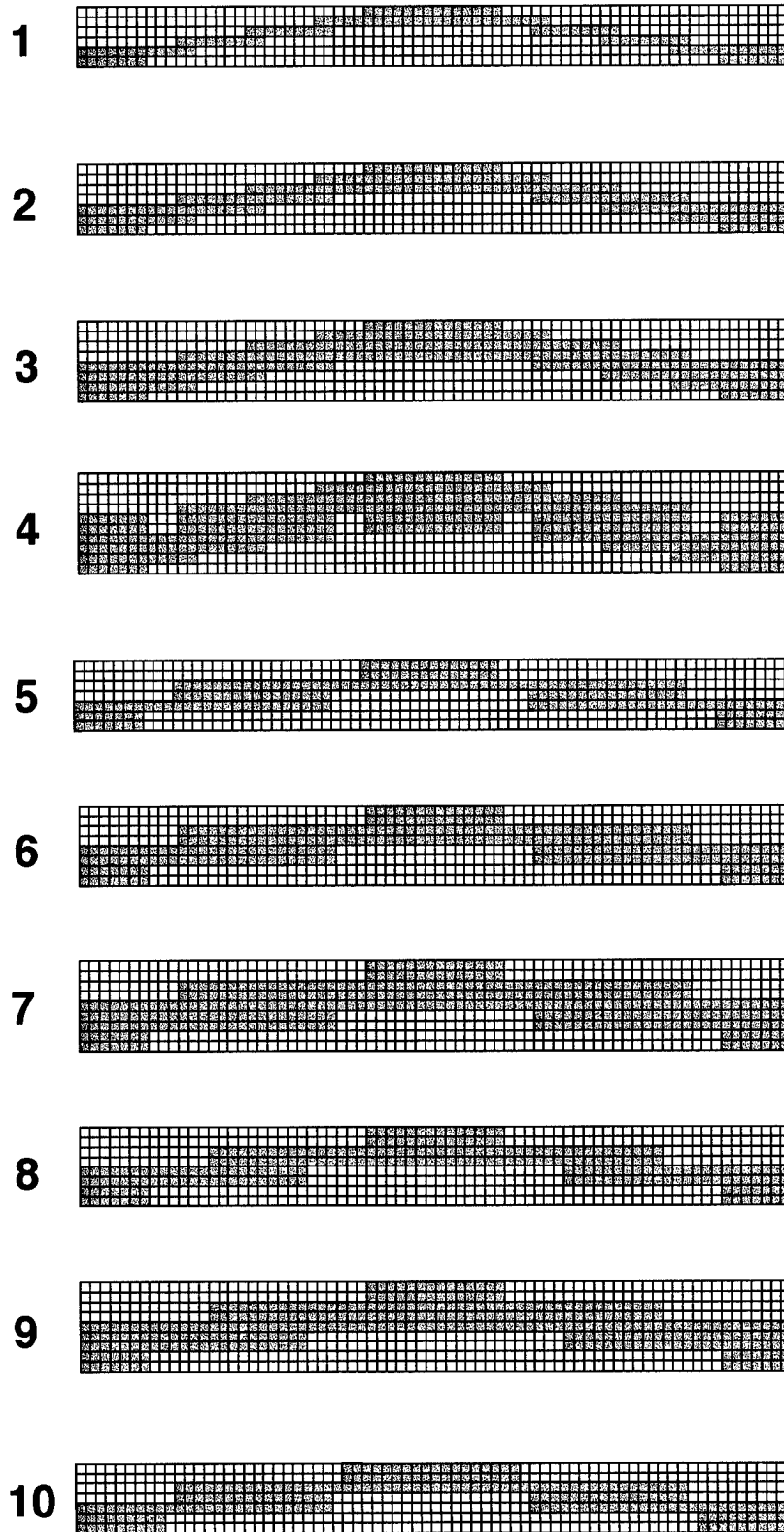


Figure 25. Modeled internal flextensional amplifier designs.

**Table 10. Performance of Candidate Internally Amplified Actuators**

Model	Displacement (mm)	Load (N)	Energy (J)	Relative Efficiency (%)
Requirement	2.946	430	1.27	
MSI-53HD Material	0.22	13400	2.90	100
Case 1 (aluminum)	1.2	16	0.02	0.7
Case 1 (steel)	2.0	30	0.06	2.0
Case 2 (aluminum)	0.9	32	0.03	1.0
Case 2 (steel)	1.6	88	0.14	4.8
Case 3 (aluminum)	0.6	56	0.03	1.1
Case 3 (steel)	1.0	140	0.13	4.7
Case 4 (aluminum)	2.0	32	0.06	2.2
Case 4 (steel)	3.4	80	0.27	9.2
Case 5 (aluminum)	2.1	72	0.15	5.1
Case 5 (steel)	3.6	180	0.65	22.0
Case 6 (aluminum)	1.2	127	0.15	5.2
Case 6 (steel)	2.0	317	0.65	21.5
Case 7 (aluminum)	0.8	223	0.19	6.1
Case 7 (steel)	1.4	558	0.80	26.5
Case 8 (aluminum)	1.2	127	0.15	5.2
Case 8 (steel)	2.0	317	0.65	21.5
Case 9 (aluminum)	0.8	223	0.15	6.1
Case 9 (steel)	1.4	140	0.20	6.6
Case 10 (aluminum)	1.5	88	0.13	4.5
Case 10 (steel)	2.5	220	0.55	18.7

The modeling indicted increased energy density by the use of stainless steel, thick flextensional layers, and curved and notched structures. Steel flextensional amplifiers gave the advantage of higher energy density, but the disadvantage of fabrication difficulty. Cases 1 – 3 were too thin, showing bowing of the amplifier during operation. Case 4 was too stiff, even with flexure notches. Cases 5 – 10 examined easily fabricated designs with various degrees of stiffness.

These internal flexures traded displacement amplification for efficiency. None of the designs were capable of meeting both the amplification and efficiency requirements. The most efficient design was Case 7. The steel design had 26 percent efficiency and would be 2 times lower in energy density

than the requirement. The aluminum design had 6.4 percent efficiency and was 7 times lower in energy density than the requirement. Both of these designs fell short of the displacement requirement.

Cases 6 and 8 showed the best balance of displacement amplification and efficiency, and both cases were capable of meeting the requirements with improvements in material microstrain and energy density. The required material microstrain capability would be 2060 and the energy density would be  $17.6 \text{ kJ/m}^3$ .

In summary, these actuator modeling, fabrication, and demonstrations showed the breadth of actuator performance possibilities available through net-shape ceramic forming and innovative actuator design. All of the design options explored showed performance trade-offs in terms of device efficiency and energy density when mechanical amplification techniques were used. No design was capable of meeting the onerous Boeing requirements. Ultimately, these devices require higher energy density piezoelectric materials to meet the helicopter rotorblade actuation performance goal. No COTS piezoelectric ceramic material comes close to having sufficient energy density for this application. The new PZN and PMN single crystal or pseudo-single crystal materials have been shown through modeling to have sufficient energy density, but await commercial development under other programs. Recognizing the limitations of COTS piezoelectric ceramics, MSI undertook with the COTR approval to develop a high energy density piezoelectric ceramic formulation suitable for program use.

## 4.4 High Energy Density Actuator Materials

### 4.4.1 Background

The major limitation of piezoelectric actuator systems is the energy density and microstrain of the piezoelectric ceramic itself. To maximize these factors, the ideal material would possess high dielectric constant, high coupling factor, and low losses under high electrical drive conditions. Currently, there are three candidate high energy density ceramics available commercially. These material types are “hard” PZT (DoD types I and III), “very soft” PZT (DoD type VI and PNN-PZT), and PMN-PT.

Since the early 1960s, the US Navy has exclusively used “hard” PZT materials for high energy density sonar applications. This application requires high velocity (actuation strain times frequency) and continuous duty cycle operation. In this operating regime, piezoelectric actuators or transducers tend to be heat rise limited due to high dielectric and mechanical losses under driving conditions (1). As such, “hard” PZT materials are capable of higher acoustic or energy outputs in these applications despite their lower dielectric and piezoelectric constants. This is due to the excellent field, pressure, and power stability of these materials, as shown in Figures 26 - 28 (2). The lower losses and better stability features of the “hard” PZT materials are achieved by reducing total domain wall motion (both ferroelectric and ferroelastic walls) by doping with acceptor dopants and by keeping the Curie temperature high ( $T_C \sim 325^\circ\text{C}$ ).

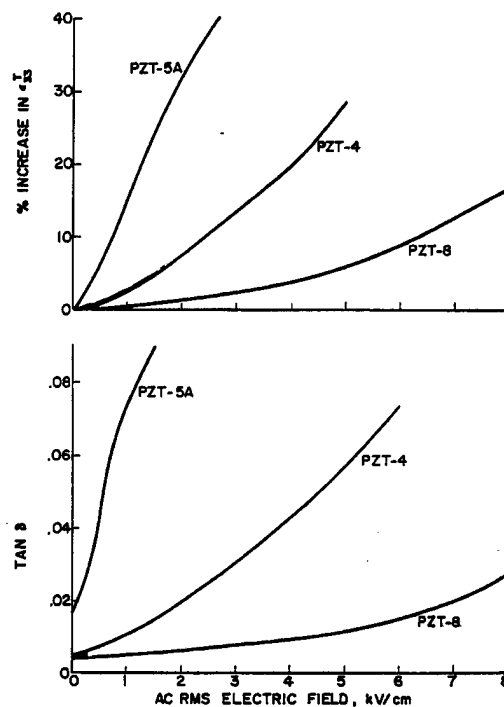


Figure 26. Percent change in dielectric constant and dielectric loss as a function of electric field for: DoD type I (PZT-4), DoD type II (PZT-5), and DoD type III (PZT-8) materials (2).

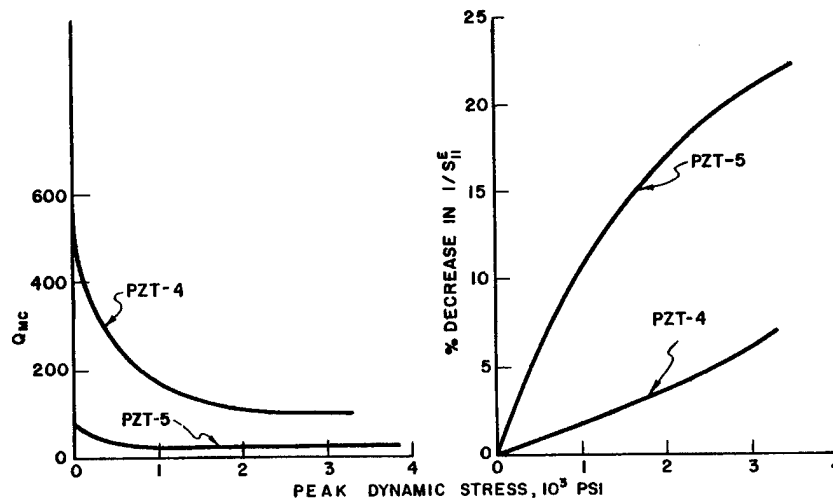


Figure 27. Stress dependence of mechanical Q and Young's modulus ( $1/s_{11}^E$ ) for DoD type I (PZT-4) and DoD type II (PZT-5) materials (2).

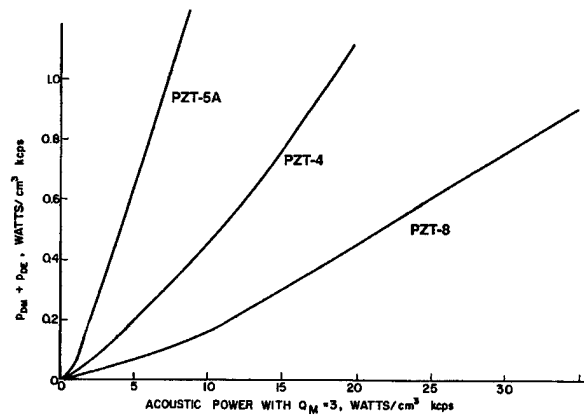


Figure 28. Total dissipated heat power ( $P_{DE} + P_{DM}$ ) as a function of the acoustic power ( $P_M$ ) for: DoD type I (PZT-4), DoD type II (PZT-5), and DoD type III (PZT-8) materials (2).

For applications requiring low velocity actuation and low duty cycle operation, actuators tend to be limited by efficiency or electromechanical energy density (1). In this case, the low losses and high stability properties of the DoD type I and III materials are not as important as high electromechanical energy density and high efficiency. As such, both "very soft" PZT (DoD type VI and PNN-PZT) and PMN-PT materials have been utilized for these applications. Both materials are also used in voltage or field-limited applications.

The rotorblade flap actuation application lies between the two limiting cases discussed above. For this application, a "hard" PZT material with improved bandwidth, electromechanical energy density, and efficiency is desirable. In order to improve these properties without significantly changing the low loss characteristics of "hard" PZT materials, the Curie temperature may be lowered by solid solution of isovalent dopants. Properly modified, this will improve bandwidth, electromechanical energy density, and efficiency, at the expense of increased losses and decreased temperature stability. Examples of common isovalent additions to PZT materials are shown in Table 11.

**Table 11. PZT Isovalent Additions**

Type	Example
$A^{+2}$	Sr Ba
$B^{+4}$	Sn
$A^{+1} A^{+3}$	$Na_{0.5} La_{0.5}$ $Na_{0.5} Bi_{0.5}$ $K_{0.5} La_{0.5}$ $K_{0.5} Bi_{0.5}$
$A^{+1} B^{+5}$	Na Nb Na Sb K Nb K Sb
$A^{+3} B^{+3}$	Bi Cr Bi Al Bi Fe La Cr La Al La Fe
$B^{+3} B^{+5}$	$Fe_{0.5} Nb_{0.5}$ $Fe_{0.5} Sb_{0.5}$ $Sc_{0.5} Nb_{0.5}$ $Sc_{0.5} Ta_{0.5}$
$B^{+2} B^{+5}$	$Ni_{1/3} Nb_{2/3}$ $Mg_{1/3} Nb_{2/3}$ $Zn_{1/3} Nb_{2/3}$ $Mg_{1/3} Ta_{2/3}$
$B^{+2} B^{+6}$	$Co_{0.5} W_{0.5}$ $Mg_{0.5} W_{0.5}$
$B^{+3} B^{+6}$	$Fe_{2/3} W_{1/3}$



However, most of these isovalent dopants adversely affect the perovskite crystal parameters including A- and B-site crystal strains and adversely change the Goldschmidt perovskite tolerance factor (3), the electronegativity (4), and the oxygen valence bond sum (5). These modifications increase internal friction and ferroelastic wall to ferroelectric wall contribution, both of which tend to increase losses and decrease temperature, pressure, and field stabilities. Table 12 shows that standard piezoelectric and electrostrictive materials tend to have low A- and B-site crystal strains and moderate perovskite tolerance factors, electronegativities, and oxygen valence bond sums. Table 13 shows that traditional isovalent doping ( $A^{+2}$  and  $B^{+2}$   $B^{+5}$ ) of DoD type I materials adversely effect the perovskite crystal parameters.

**Table 12. Perovskite Crystal Parameters of Standard Piezoelectric And Electrostrictive Materials**

Material	A-Site Strain	B-Site Strain	Perovskite Tolerance Factor	Electronegativity Difference	Oxygen Bond Valence Sum
DoD I	0.21	-0.01	1.0073	1.9118	1.8401
DoD II	0.00	-0.13	1.0029	1.8786	1.8084
DoD V	1.76	-0.06	1.0061	1.9203	1.8357
DoD VI	-1.08	-0.13	1.0012	1.9210	1.8437
DoD III	0.28	-0.05	1.0083	1.9020	1.8383
E/S PMN	-0.17	-0.92	1.0087	1.8722	1.7535
P/E PMN	0.00	-2.16	1.0207	1.8608	1.7715
PNN	0.00	-0.80	1.0182	1.8161	1.7835
"Ideal" PZT Range	0 to 0.3	0 to -0.2	1.007 to 1.010	1.88 to 1.92	1.83 to 1.84

**Table 13. Perovskite Crystal Parameters for Traditionally Doped DoD Type I Materials**

Isovalent Addition	A-Site Strain	B-Site Strain	Perovskite Tolerance Factor	Electronegativity Difference	Oxygen Bond Valence Sum
Sr	-0.90	0.00	1.0035	1.9163	1.8414
Ba	1.76	0.00	1.0126	1.9483	1.8577
PNN	0.00	-0.09	1.0107	1.8472	1.8039
PMN	0.00	-0.58	1.0271	1.8868	1.7503
PZN	0.00	-0.80	1.0070	1.8435	1.7913

In order to take advantage of the lower Curie temperature, isovalent additions must be made to minimize internal friction and increase ferroelectric wall to ferroelastic wall contribution. Perovskite stabilizers and "hardeners"  $A^{+2}$  and  $B^{+4}$ , such as  $PbTiO_3$ ,  $BaTiO_3$ , and  $SrTiO_3$ , are well known in the development and manufacture of PZT, PMN and PZN materials. Ikeda and Okano (6) showed improved piezoelectric properties with improvements in dielectric loss and internal friction with selected  $A^{+3} B^{+3}$  modifications of PZT. Small B1-B2 size difference in  $B^{+2} B^{+5}$  and  $B^{+3} B^{+5}$  materials have been shown to reduce crystal strain, as observed by the increased ordering tendency of PNN material over PMN and PZN materials.

The development of PZT-4S material also indicated that stability is gained by smaller-sized, low-size-difference A- and B-site dopants in PZT (7, 8). The PZT-4S formulation exhibits wider bandwidth, higher energy output, greater efficiency, and greater temperature stability than other DoD type I materials. Figure 29 shows that PZT-4S formulation exhibit a high coupling factor. In addition, it retains its properties or polarization to a significantly higher temperature, even though its Curie temperature is similar to the other compositions. Figures 30 - 32 show that its actuation properties (microstrain, block pressure, and energy density) also exhibit an exponential temperature dependency, whereas the other compositions remain flat due to partial depolarization. Theory predicts an exponential temperature dependency due to property dependency on thermally activated domain wall motion.

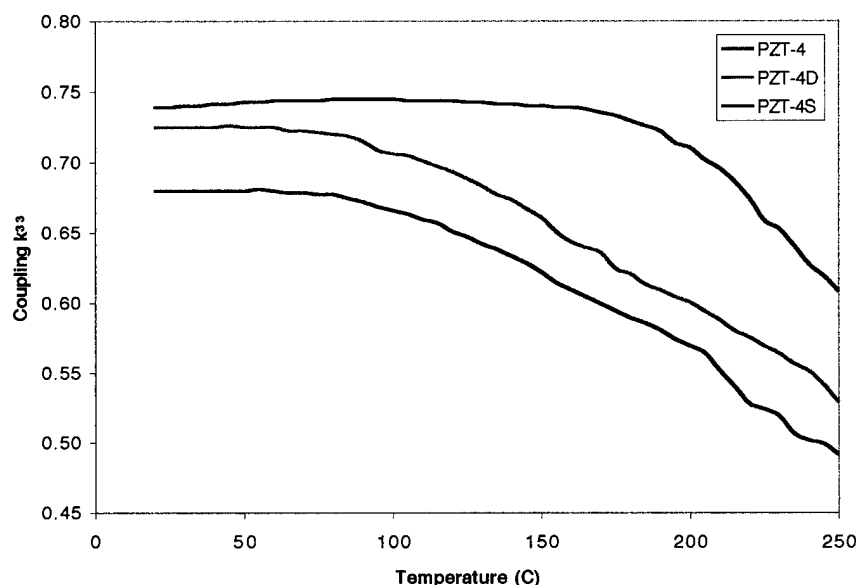


Figure 29. Piezoelectric coupling factor  $k_{33}$  as a function of temperature for various DoD type I materials.

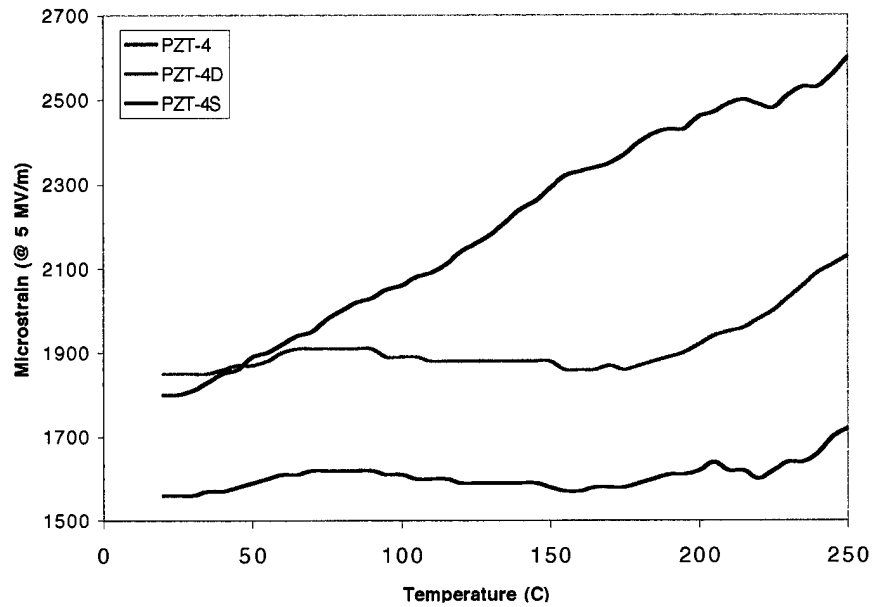


Figure 30. Microstrain capability (at 5 MV/m) as a function of temperature for various DoD type I materials.

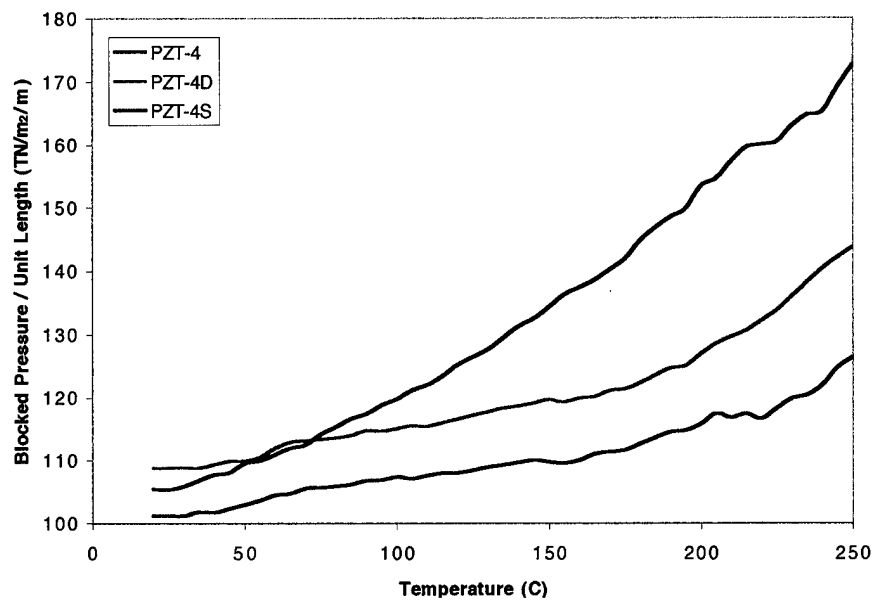


Figure 31. Blocked pressure (per unit length at 5MV/m) as a function of temperature for various DoD type I materials.

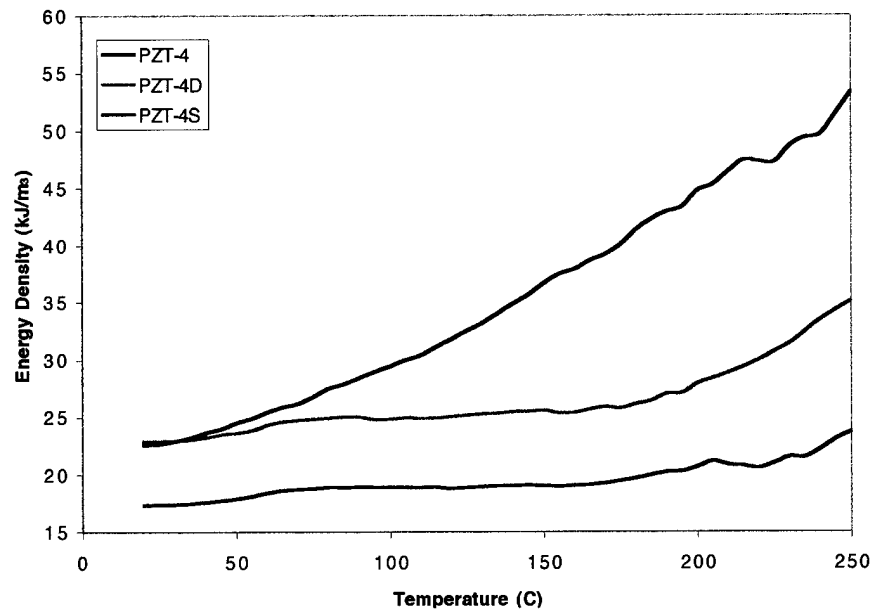


Figure 32. Energy density (at 5 MV/m) as a function of temperature for various DoD type I materials.

#### 4.4.2 New Material Development

To further improve the actuation characteristics of “hard” PZT materials, the Curie temperature ( $T_c$ ) may be lowered to the level similar to the “very soft” PZT materials. To estimate the effect of this change, the elevated temperature properties of DoD type I may be compared. Table 14 shows measured properties of the various DoD type I materials at both room temperature and an elevated temperature equivalent to a material with a 190°C Curie temperature. Only PZT-4S shows a significantly higher energy density at the elevated temperature.

**Table 14. Room and Elevated Temperature Properties of Various DoD Type I Materials (7, 8)**

Property	Units	PZT-4		PZT-4D		PZT-4S	
		RT	150°C	RT	130°C	RT	130°C
$K_{33}^T$		1355	1776	1576	1954	1494	2173
$k_{33}$		0.70	0.62	0.73	0.68	0.74	0.74
$d_{33}$	pm/V	312	316	369	356	360	437
$Y_{33}^E$	GN/m <sup>2</sup>	61.3	69.5	58.8	62.6	58.5	58.6
Microstrain		1560	1580	1850	1780	1800	2185
Blocked Pressure	TN/m <sup>2</sup> /m	96	110	109	111	105	128
Energy Density ( $k_{33}^2 \epsilon_{33}^{-1} E^2$ )	kJ/m <sup>3</sup>	18.4	19.0	22.9	25.3	22.6	33.2
$T_c$	°C	320	190	300	190	300	190

Therefore, an appropriate isovalent doping is required to achieve a high energy density “hard” PZT material. The three best dopant approaches include certain isovalent  $A^{+2}$ ,  $B^{+3} B^{+5}$ , and  $A^{+3} B^{+3}$  solid solutions. These dopants maintain low A- and B-site crystal strains as well as maintaining perovskite tolerance factors, electronegativities, and oxygen valence bond sums in the range of traditional DoD type I and III materials. Table 15 shows the perovskite crystal parameters of PZT material with these isovalent dopants.

**Table 15. Perovskite Crystal Parameters for Isovalently Doped DoD Type I Materials**

Material	Dopant Approach	A-Site Strain	B-Site Strain	Perovskite Tolerance Factor	Electronegativity Difference	Oxygen Bond Valence Sum
Approach 1	$A^{+2}$	0.29	-0.01	1.0071	1.9207	1.8208
Approach 2	$B^{+3} B^{+5}$	0.28	-0.42	1.0107	1.8841	1.8338
Approach 3	$B^{+3} B^{+5}$	0.28	-0.14	1.0091	1.8949	1.8345

The resultant properties of these isovalently-doped materials are shown in Table 16. Approach 2 material meets or exceeds most of the goal properties. Of particular interest are its high  $k_{33}$  (estimated) and  $d_{33}$  values. If its assumed electric field limit is correct, this material has 1.7 and 2.8 times the microstrain and energy density capability, respectively, over MSI-53HD material. It should be noted that both approaches 1 and 3 have low piezoelectric values since the property peak at the morphotropic phase boundary had not been reached. As shown in Figures 33 and 34, both approaches 2 and 3 show appropriate reductions in Curie temperature and excellent peak dielectric constant. As such, both approaches 2 and 3 should be considered for any future material development. Approach 1 had a Curie temperature and peak dielectric constant too low to consider for any future development. As shown in Figure 35, approach 2 also exhibited the same dielectric constant behavior as a  $T_C$  reduced PZT-4S material, demonstrating the use of an appropriate isovalent dopant. Since approach 3 had a higher dielectric constant peak, this material may exhibit better piezoelectric properties at its compositional peak than approach 2.

**Table 16. Properties of Newly Developed Low  $T_C$  Hard Piezoelectric Materials**  
(values in italics are estimated)

Property	Units	PZT-4	Goal	Approach 1	Approach 2	Approach 3
$K_{33}^T$		1355	2175	1726	1750	1838
$\tan \delta$		0.003	0.005	0.003	0.006	0.007
Qm		550	250	400	250	250
$k_{33}$		0.70	0.74	<i>0.57</i>	<i>0.73</i>	<i>0.59</i>
$k_p$		0.56	0.64	0.44	0.61	0.46
$k_{31}$		0.33	0.38	0.26	0.36	0.27
$d_{33}$	pm/V	312	440	318	495	288
$d_{31}$	pm/V	128	193	102	163	123
$Y_{33}^E$		65	60			
$Y_{11}^E$	GN/m <sup>2</sup>	81	74	96	75	80
$T_C$	°C	320	250	200	240	230
Assumed Field Limit	MV/m	5	5	5	5	5
Free Microstrain		1560	2200	1590	2475	1440
Blocked Pressure	TN/m <sup>2</sup> /m	101	132			
Energy Density	kJ/m <sup>3</sup>	18.4	33.0	15.5	25.8	17.7

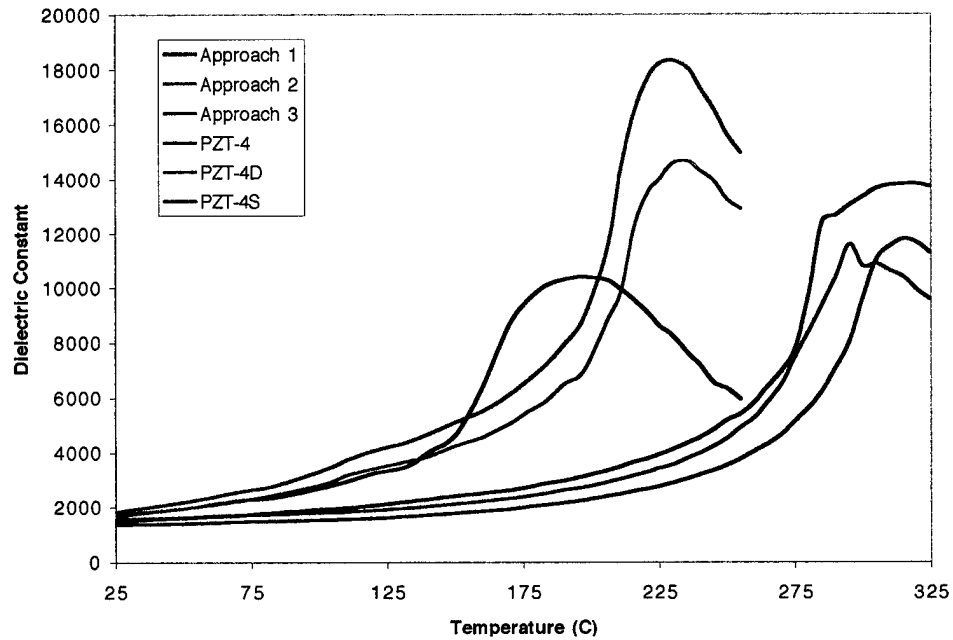


Figure 33. Dielectric constant as a function of temperature for various DoD type I and newly developed materials.

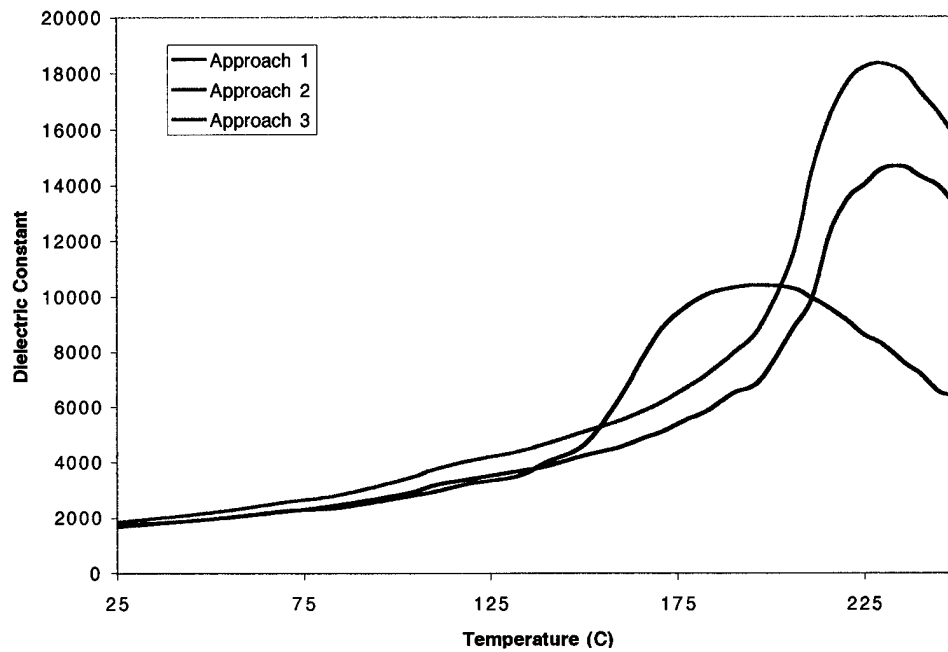


Figure 34. Dielectric constant as a function of temperature for newly developed materials.

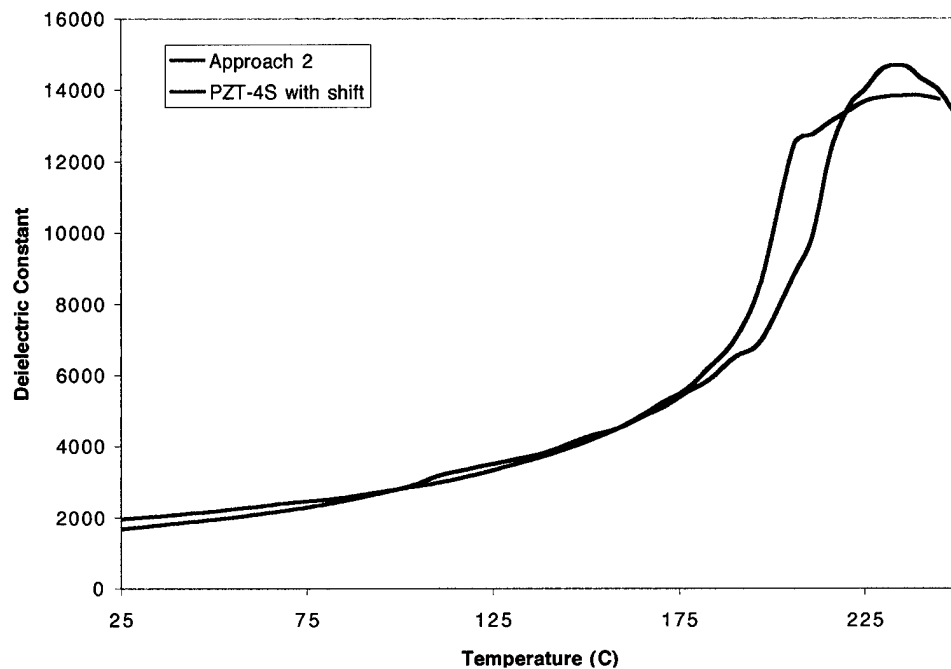


Figure 35. Dielectric constant as a function of temperature for newly developed “approach 2” and PZT-4S materials, with PZT-4S Curie temperature shifted to 240°C.



#### **4.5 Hybrid Multilayer Actuator**

Based on their inherent high energy density, stacked co-fired  $d_{33}$  multilayer actuators were developed to meet the specifications established by Boeing Mesa. These specifications were based on the Boeing flexural and the MIT X-frame mechanical amplifier designs. The specifications assume that these mechanical amplifiers are at least 48% efficient. In order to meet these specifications, MSI designed, manufactured, and tested hybrid multilayer actuators from both MSI-53HD and PNN-1 materials. These actuator designs are compared to the specifications in Table 17.

**Table 17. Multilayer Piezoelectric Actuator Specifications and MSI Actuator Designs**

Property	Boeing Mesa Requirement	MSI-53HD Design	PNN-1 Design
Cross-section (mm)	12.7 mm	12.7	12.7
Length (mm)	$\geq 18$ mm	20	20
Maximum Voltage (V)	150 – 500	225	180
Free Microstrain	$\geq 1500$	1410	1450
Blocked Force (kN)	$\geq 10$	10.3	8.7
Energy Density ( $\text{kJ/m}^3$ )	$\geq 8.2$	7.9	10.0

The hybrid actuators consisted of seven bonded co-fired segments. Each co-fired segment consisted of twenty-five  $115 \mu\text{m}$  layers. Per the requirement, these multilayer actuators were terminated on one side. Actuators were designed and manufactured with both MSI-53HD and PNN-1 materials. The properties of these materials are given in Table 18.

**Table 18. Properties of MSI-53HD and PNN-1 Materials**

Property	Units	MSI-53HD	PNN-1
$K_{33}^T$		3600	6230
$k_{33}$		0.76	0.80
$d_{33}$	pm/V	725	930
$Y_{33}^E$	$\text{GN/m}^2$	50	42
$T_c$	$^{\circ}\text{C}$	220	140
Assumed Field Limit	MV/m	2	1.6
Free Microstrain		1450	1490
Blocked Pressure	$\text{TN/m}^2/\text{m}$	73	62
Energy Density	$\text{kJ/m}^3$	9.2	11.6

As illustrated in Figure 36, the co-fired segments were manufactured using tape cast ceramic sheets onto which internal platinum electrodes were screen-printed. After printing, the layers were stacked and laminated. The resultant multilayer structure was fired in the conventional manner. After firing, the sides were lapped to expose the inner electrodes, and these were terminated down one side with an external chrome-gold electrode. The segment was then polarized. The actuator stack was assembled from seven segments, which were glued together. Beryllium copper electrodes were used between each segment. Lead wires were soldered to these metal electrodes. Co-fired multilayer segment and as assembled hybrid MSI-53HD stack actuator before lead attachment is shown in Figure 37. The hybrid actuators were then tested for piezoelectric and actuation properties.

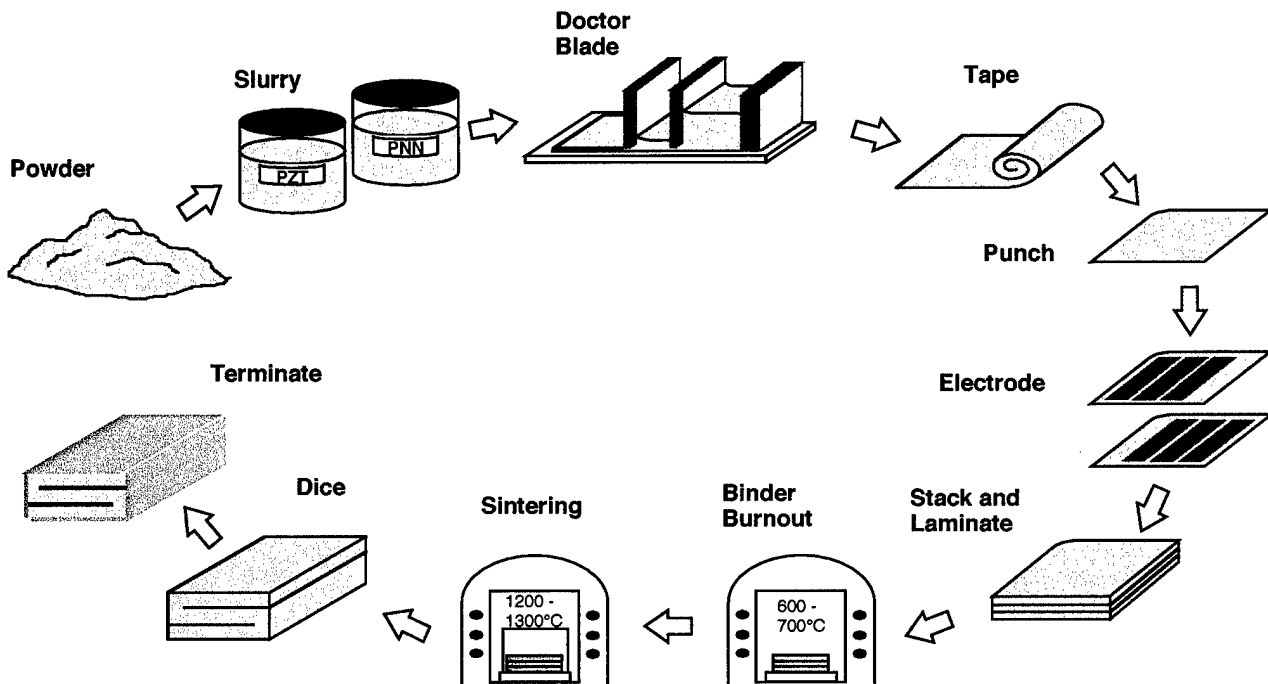


Figure 36. Co-fired multilayer segment fabrication process.

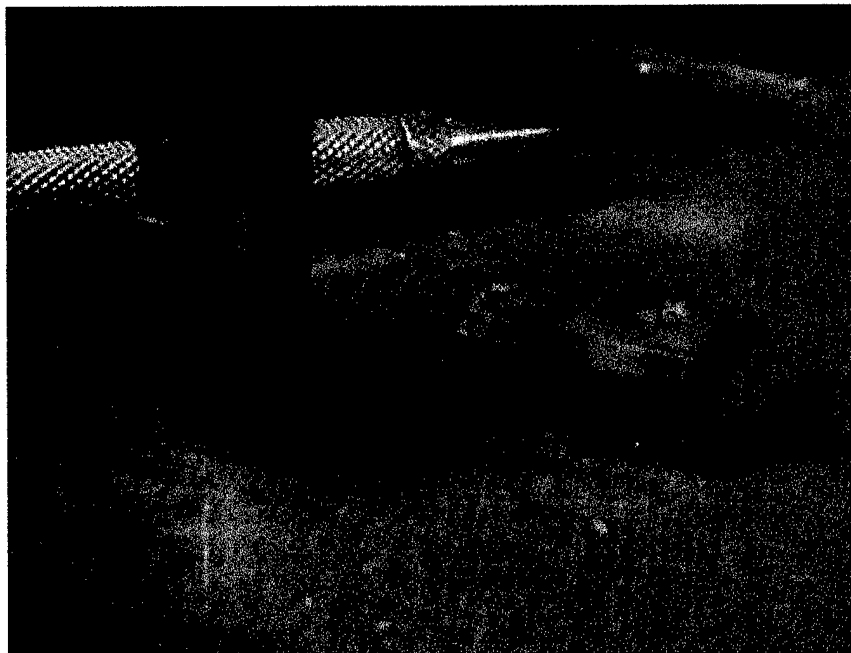


Figure 37. A 12.7 x 12.7 x 20 mm hybrid  $d_{33}$  multilayer actuator consisting of seven 25 layer co-fired segments were produced and tested. A stack actuator (left) and several co-fired segments (right) are shown.

## **5.0 Conclusions**

Due to its relatively high frequency, high energy density, and wide bandwidth requirements, the rotorblade trailing edge flap requires a large displacement, high energy density piezoelectric actuator. Compared with state-of-the-art multilayer piezoelectric actuators, the rotorblade flap actuator requires thirteen times the strain capability at 55% of the total energy available, representing a considerable challenge given the current state-of-the-art. In order to meet the requirements of this application, MSI evaluated several novel actuation approaches, including piezocomposite volume, linear serpentine, and internally amplified multilayer actuators. All of these approaches fell short of meeting the requirements. The best approach was an internally amplified multilayer, which was 26 percent efficient and two times lower in displacement and energy density than the requirement. In order to use the internally amplified design, an improved piezoelectric material was required. Improvements of about 150 percent and 200 percent were required for the microstrain and energy density, respectively, over state-of-the-art MSI-53HD COTS material. Initial development of a new high energy density material showed the potential for meeting these requirements with improvements of 1.7 and 2.8 times the microstrain and energy density respectively over MSI-53HD material.

In order to achieve the required actuator performance, the new high energy density material must be fully developed and its operational limitations determined. Co-fired multilayer technology must then be developed for this new material. The multilayer actuators could then be evaluated with the Boeing flexure, the MIT X-frame, or the internal flextensional mechanical amplifier designed in this program.

Specific program accomplishments include:

- Designed, fabricated, and tested a subscale volume actuator, offering ruggedness, high volume efficiency, and easily redirected actuation direction.
- Designed, scaled-up, fabricated, and tested over 200 unidirectional serpentine actuator elements, 25 x 25 x 1 mm in size.
- Demonstrated serpentine actuator with 4 times free displacement improvement over  $d_{33}$  multilayer devices.
- Designed and evaluated an internally amplified multilayer actuator, with efficiencies as high as 24%.
- Designed, fabricated, and tested stacked co-fired multilayer actuators manufactured with MSI-53HD and PNN-1 materials.
- Developed a new high energy density actuator material, with potentially 1.7 and 2.8 times higher microstrain and energy density compared with state-of-the-art COTS piezoelectric ceramic materials.
- Showed the potential for meeting the helicopter rotorblade actuation requirements performance with the internally amplified multilayer actuator with the new high energy density material.

## **6.0 Appendices**

### **Appendix A. References**

1. D. A. Berlincourt, "Power Capacities of Piezoelectric Ceramics in Sonar-Type Acoustic Transducers," Morgan Matroc Inc. Technical Paper TP-221, Bedford, OH.
2. D. A. Berlincourt and H. H. A. Krueger, "Behavior of Piezoelectric Ceramics Under Various Environmental and Operation Conditions of Radiating Sonar Transducers," Morgan Matroc Inc. Technical Paper TP-228, Bedford, OH.
3. V. M. Goldschmidt, "Geochemische Verteilungsgesetze der Elements," Skr. Norske Vidensk Akad. Kl., No. 2 (1926), No. 8 (1927).
4. L. Pauling, "The Nature of the Chemical Bond," 3<sup>rd</sup> Edition, Cornell University Press, Ithaca, N.Y. (1960).
5. N. Wakiya, K. Shinozaki, and N. Mizutani, "Estimation of Phase Stability in  $\text{Pb}(\text{Mg}_{1/3}\text{Nb}_{2/3})\text{O}_3$  and  $\text{Pb}(\text{Zn}_{1/3}\text{Nb}_{2/3})\text{O}_3$  Using the Bond Valence Approach," J. Am. Ceram. Soc. 80 [12] 3217-20 (1997).
6. T. Ikeda and T. Okano, "Piezoelectric Ceramics of  $\text{Pb}(\text{Zr-Ti})\text{O}_3$  Modified by  $\text{A}^{1+} \text{B}^{5+} \text{O}_3$  or  $\text{A}^{3+}\text{B}^{3+}\text{O}_3$ ," Jpn J Appl. Phys. 3 (2) 63-71 (1964).
7. C. D. Near, T. J. Meyer, and S. Sprungl, "New "Hard" PZT Ceramics," presented at the 22<sup>nd</sup> Annual Ultrasonics Industry Association meeting, June 1991, New York, NY.
8. C. D. Near, T. J. Meyer, and S. Sprungl, "Design and Characterization of New "Hard" PZT Ceramics," presented at the 93<sup>rd</sup> Annual American Ceramic Society meeting, May 1991, Cincinnati, OH.

## **Appendix B. Presentations and Publications**

### **Presentations**

March 5, 1997	Presentation	SPIE Smart Structures & Materials Conference, CA
Nov. 3, 1997	Presentation	ONR meeting, DC
Nov. 7, 1997	Presentation	DARPA Review, VA
Feb. 10, 1998	Presentation	DARPA meeting, MA
Feb. 25, 1998	Presentation	Boeing Phantom Works, MO
Feb. 26, 1998	Presentation	NAVSEA
March 1-5, 1998	Presentation	SPIE Smart Structures & Materials Conference, CA
April 22, 1998	Presentation	MIT meeting, MA
May 12-14, 1998	Presentation	ONR Review, PA
June 8-11, 1998	Presentation	DARPA Review, VA
June 19, 1998	Presentation	ONR MURI Review, DC
Nov. 17, 1998	Presentation	Delphi, MI
March 1 – 5, 1999	Presentation	SPIE Smart Structures & Materials Conference, CA
April 13 – 15, 1999	Presentation	ONR Review Meeting, PA
June 17-18, 1999	Presentation	DARPA Review, VA

### **Publications**

C. Near et al, "Injection molded PZT actuators," SPIE Smart Structures and Materials Conference, March 1998.